

Modeling and Simulation of Fusion Plasma Thrusters with Magnetohydrodynamics

Modellierung und Simulation von Fusionsplasmatriebwerken mit Magnetohydrodynamik

Nikolaos Perakis

Bachelor Thesis
Physik-Department
Technische Universität München



Supervisors: Prof. Ulrich Stroth
Prof. Eric Sonnendrücker
Dr. Florian Hindenlang

Date of submission: July 08, 2015

Max Planck Institute for Plasma Physics
Department of Numerical Methods in Plasma Physics

2015

Aknowledgements

I would like to thank my supervisor Dr. Florian Hindenlang for his constant support throughout the 3 months of the thesis. I really appreciate the time he invested in the project and the interest he demonstrated during our fruitful discussions, always eager to share his advice and try to tackle the issues I encountered. Additionally, I would like to express my gratitude to all developers of the solver Flexi for making this infrustructre available to me, thereby accelerating my progress in the beginning of the project.

I would also like to thank Prof. Stroth and Prof. Sonnendrücker for allowing me to carry out my thesis within the Max Planck Institute and all colleagues at the Department of Numerical Methods for their ideas and comments.

Last but not least, I want to thank all members of the Icarus Interstellar organisation for inspiring me to come up with the topic of the thesis and for motivating me to combine the topics of plasma physics and interstellar travel.

Munich, July 08 2015

Nikolaos Perakis

Contents

Acknowledgements	iii
Contents	v
Symbols and Abbreviations	vii
Abstract	xi
1. Introduction	1
1.1. Overview of Space Propulsion	1
1.2. Fusion Propulsion	4
1.2.1. Nuclear Fusion	4
1.2.2. Fusion Confinement	7
1.2.3. Fusion Propulsion Considerations	9
1.2.4. Magnetic Nozzle	11
2. Modeling and Numerics	13
2.1. Magnetohydrodynamics	13
2.1.1. MHD with external field	15
2.1.2. Waves in MHD	16
2.2. Finite Volume Methods	21
3. Initialization	25
3.1. Conditions after Ignition	25
3.2. Developed Initial Conditions	27
3.2.1. Pressure of the plasma	28
3.2.2. Velocity of the plasma	28
3.3. Gas dynamic investigation of initialization uncertainty	29
3.3.1. Density of surrounding environment	30
3.3.2. Pressure of surrounding environment	33
3.4. Initial velocity profile	35
3.4.1. Uniform disc initialization	35

3.4.2. Linear profile disc initialization	38
4. Results	45
4.1. Constant magnetic field	45
4.1.1. Comparison of initializations	45
4.1.2. Modification of outer pressure	51
4.1.3. Presence of MHD waves	52
4.1.4. Effect of velocity	54
4.1.5. Efficiency of nozzle	56
4.2. Coil magnetic field	59
4.2.1. Sponge layer	62
4.2.2. Geometry modification	64
5. Conclusion	71
A. 1D Simulation of velocity discontinuity	73
B. Calculation of efficiency for constant field	77
C. Meshes	79
Bibliography	83
List of Tables	87
List of Figures	87

Symbols and Abbreviations

Symbols

I_{sp}	Specific impulse [s]
\dot{m}	Mass flow rate [kg/s]
F	Thrust [N]
g_0	Gravity acceleration [m/s^2]
τ_e	Confinement time [s]
W	Volumetric plasma energy [J/m^3]
P_{loss}	Volumetric plasma energy loss rate [W/m^3]
n	Plasma number density [m^{-3}]
k_B	Boltzmann's constant [J/K]
T	Temperature [K]
σ	Reaction cross section [m^2]
v	Velocity magnitude [m/s]
\mathbf{v}	Velocity vector [m/s]
E_{ch}	Energy of reaction products [J]
G	Fusion energy gain [–]
E_{fusion}	Power produced in fusion [W]
E_{heat}	External power input [W]
η_{nozzle}	Efficiency of nozzle [–]
ρ	Density [kg/m^3]
v_x	Velocity along x direction [m/s]
v_y	Velocity along y direction [m/s]
V	Volume [m^3]
U	Vector of conservative variables
\mathbf{F}^a	Advection flux
$\tilde{\mathcal{E}}$	Total volume specific energy of fluid [J/m^3]
$\tilde{\mathcal{E}}_T$	Thermodynamic volume specific energy of fluid [J/m^3]

$\tilde{\mathcal{E}}_K$	Kinetic volume specific energy of fluid [J/m ³]
$\tilde{\mathcal{E}}_M$	Magnetic volume specific energy of fluid [J/m ³]
$\tilde{\mathcal{E}}_{in}$	Perturbation energy of fluid [J/m ³]
\mathbf{B}	Magnetic field vector [T]
\mathbf{B}_0	External magnetic field vector [T]
\mathbf{B}_{in}	Induced magnetic field vector [T]
p	Thermodynamic pressure [N/m ²]
\tilde{p}	Sum of thermodynamic and magnetic pressure [N/m ²]
\tilde{p}_{in}	Perturbation pressure [N/m ²]
γ	Heat capacity ratio [-]
μ_0	Magnetic permeability constant [H/m]
S	External sources
$\underline{\underline{\mathbf{I}}}$	Identity tensor [-]
\mathbf{j}	Current density [A/m ²]
v_S	Speed of sound [m/s]
v_A	Alfven speed [m/s]
v_M	Magnetosonic speed [m/s]
v_ϕ	Phase velocity [m/s]
\mathbf{k}	Wave vector [m ⁻¹]
\mathbf{e}_n	Normal unit vector [-]
\mathbf{e}_t	Tangential unit vector [-]
s	Coordinate along curved field line [m]
R	Radius of curvature of field line [m]
ω	Wave angular frequency [s ⁻¹]
θ	Angle [deg]
A	Area [m ²]
\mathbf{n}	Surface normal vector [-]
λ_{max}	Highest wave speed [m/s]
Δx	Spatial increment [m]
r_p	Plasma initial radius [m]
R_c	Coil radius [m]
I	Coil current [A]
Z	Atomic number [-]

q	Ion charge [C]
m	Plasma mass [kg]
M	Molar mass [kg/mol]
R_{gas}	Gas constant [J/(mol · K)]
N	Number of ions [-]
\bar{v}	Average ion speed [m/s]
Ma	Gas dynamic Mach number [-]

Abbreviations

1D, 2D, 3D	one, two, three dimensions / -dimensional
ICF	Inertial Confinement Fusion
NIF	National Ignition Facility
IEC	Inertial Electrostatic Confinement
MTF	Magnetized Target Fusion
VISTA	Vehicle for Interplanetary Transport Applications
NASA	National Aeronautics and Space Administration
MHD	Magnetohydrodynamics
PIC	Particle In Cell
SPH	Smoothed Particle Hydrodynamics
PDE	Partial Differential Equation
ODE	Ordinary Differential Equation
FVM	Finite Volume Method
LF	Lax-Friedrichs
UHV	Ultra High Vacuum

Abstract

The goal of this thesis is to evaluate the model of ideal MHD for the simulation of plasma flows in fusion plasma thrusters. A fusion plasma thruster is a propulsion system based on the deflection of ionized fusion products within a strong external magnetic field.

The necessity for shorter durations of interplanetary and interstellar missions renders the concept of fusion thrusters attractive due to their high specific impulse. Interstellar missions using fusion thrusters based on the concept of inertial confinement as their main propulsion system are being designed by the ICARUS project. In order to evaluate the performance of these engines and to optimize their thrust to weight ratio, different modeling techniques have been used in previous studies, involving particle or fluid descriptions of the engine plasma.

In this work, the plasma flow is modeled with the ideal MHD equations. The solution exhibits strong shock fronts and therefore the simulations are carried out with a Finite Volume method. The difference of the MHD model to other modeling techniques will be investigated.

The spatial scales of the ignition process of the inertial fusion are too small to be simulated directly, and therefore adequate initial conditions from an expanded state are necessary to start the MHD simulation. An overview of the inertial confinement fusion process is given and macroscopic initial conditions are derived via energy considerations. After modifying the initial conditions in order to incorporate them into the ideal MHD formulation, the expansion of the plasma in the absence of the magnetic field is examined. Upon identification of the critical points, simulations with a constant magnetic field are included, to evaluate the interaction of the expanding plasma and an external field. Finally, the field produced by electromagnetic coils is modeled and applied to the simulation. Numerical instabilities are encountered due to the strong coupling of the plasma motion with gas dynamic phenomena, which leads to shocks with high intensity, at the high velocities needed for plasma thrusters.

1. Introduction

1.1. Overview of Space Propulsion

The main idea behind propulsion systems lies in the acceleration of an exhaust mass, in order to impart a force onto the engine, which according to Newton's third law is directed opposite to the flow of the ejected mass. The main physical entities which characterize the thrust of the propulsion system are the mass flow rate of the propellant \dot{m} and its effective exhaust velocity v_e . The thrust is defined as:

$$F = \dot{m}v_e \tag{1.1}$$

Another equivalent formulation of the thrust, involves the specific impulse I_{sp} instead of the exhaust velocity. This is defined as the total impulse per unit weight of propellant.

$$I_{sp} = \frac{\int \dot{m}v_e dt}{\int \dot{m}g_0 dt} = \frac{v_e}{g_0} \tag{1.2}$$

g_0 stands for the acceleration of gravity on the surface of the earth. Hence the thrust can be re-defined as

$$F = \dot{m}I_{sp}g_0 \tag{1.3}$$

Mankind's space propulsion options are mainly based on chemical engines, which take advantage of the fuel's reaction enthalpy during chemical combustion. With the excess energy, the propellant (which can initially be either in solid, liquid or gaseous form) is accelerated through a nozzle, where its thermal energy is transformed to kinetic one. According to Newton's third law, an impulse is imparted onto the rocket engine, which is therefore propelled in the opposite direction of the exhaust mass. Although these conventional rockets have been proven to be reliable and effective for missions in the vicinity of the earth, their main disadvantage (low specific impulse) is evident for missions deeper into the solar system [32]. An example of a launcher system based on



Figure 1.1.: Lift-off of Ariane 5 rocket (Image from: www.esa.int)

chemical propulsion is Europe's Ariane 5 as shown during lift-off in Fig. 1.1

More efficient methods of propulsion involve electromagnetic thrusters. By accelerating ions with electromagnetic fields, high exhaust speeds can be achieved, but the resulting thrust is limited mainly due to repulsive Coulomb potential between the ions. Several interplanetary missions, like NASA's Dawn mission to the asteroid Ceres [24], have used state of the art electric propulsion engines, allowing orbits of higher energies to be reached via low thrust maneuvers. Fig. 1.2 shows the NSTAR engine on board of the Dawn spacecraft during operation.

An overview of different propulsion mechanisms and their performance characteristics can be given in [32]. The propulsion systems with the highest Technology Readiness Level are presented in Fig. 1.3.

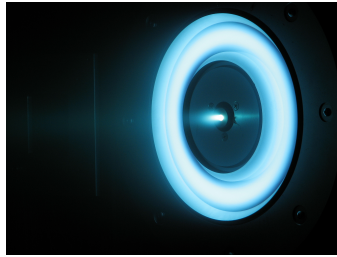


Figure 1.2.: Dawn spacecraft's NSTAR electrostatic ion thruster (Image from: www.jpl.nasa.gov/)

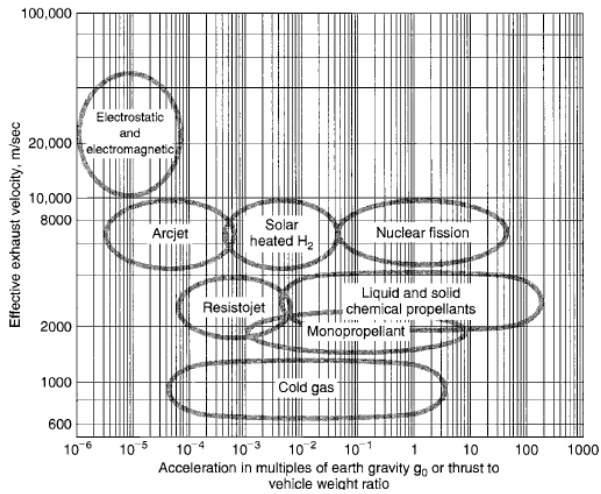


Figure 1.3.: Overview of conventional space propulsion systems [32]

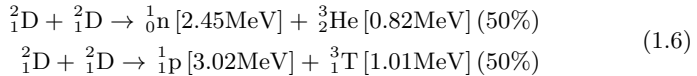
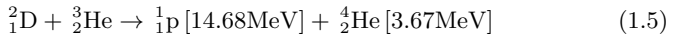
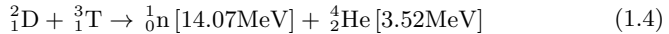
1.2. Fusion Propulsion

With the prospect of reaching other solar systems within reasonable trip durations, alternative means of propulsion have to be used, which combine a high thrust with a small fuel consumption (high specific impulse). The most prominent candidate suitable for such a mission is fusion propulsion. A fusion rocket is a theoretical design for a rocket driven by fusion power which could provide efficient and long-term acceleration [15]. The design relies on the development of fusion power technology, which currently exceeds the technological capabilities of mankind.

1.2.1. Nuclear Fusion

Just like in the concept of nuclear fusion for power generation, fusion rockets take advantage of the binding energy which is set free when two (or more) atomic nuclei collide and join to form a new type of nucleus. The unconventionally high specific impulse of these engines stems from the velocities of the ions which result from the difference in binding energy between the initial and the daughter nuclei.

Characteristically, the key reactions with the highest fusion cross sections involve [18]:



The figures in brackets stand for the kinetic energies of the corresponding ions after the fusion reaction. The cross section of these fusion reactions over a wide energy range are given in Fig. 1.4. It can be observed that D-T fusion exhibits the highest cross section.

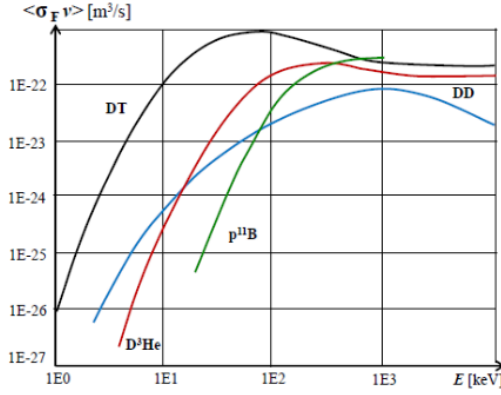


Figure 1.4.: Cross section of fusion reactions over ion temperature [13]

To sustain a fusion reaction, the plasma must be confined. The confinement time τ_e represents the rate at which the system loses energy to its environment and is given by:

$$\tau_e = \frac{W}{P_{loss}} \quad (1.8)$$

W stands for the energy density and P_{loss} measures the volumetric energy loss of the plasma. A quantitative approach to the required conditions for the plasma to reach sufficient confinement leading to an ignition is given by Lawson's criterion [21]. This is a reformulation of the condition that fusion heating should exceed the losses and combines the number density n of the plasma and the confinement time to a figure of merit describing the ignition:

$$n\tau_e \geq \frac{12k_B T}{E_{ch} \langle \sigma v \rangle} \quad (1.9)$$

In Eq. 1.9 k_B stands for Boltzmann's constant, T is the temperature, E_{ch} the energy of the reaction products that can heat up the plasma (neutrons are not included), σ the cross section of the reaction and v the relative velocity of the parent nuclei. The notation $\langle \sigma v \rangle$ is used for the average of the product σv .

1. Introduction

A further useful figure is the fusion triple product [18], which poses an extension of the Lawson criterion. In this case, the inequality also contains the temperature, leading to

$$n\tau_e T \geq \frac{12k_B T^2}{E_{ch} \langle \sigma v \rangle} \quad (1.10)$$

The theoretical triple product condition for the different fusion reactions is illustrated in Fig. 1.5 for a range of temperatures.

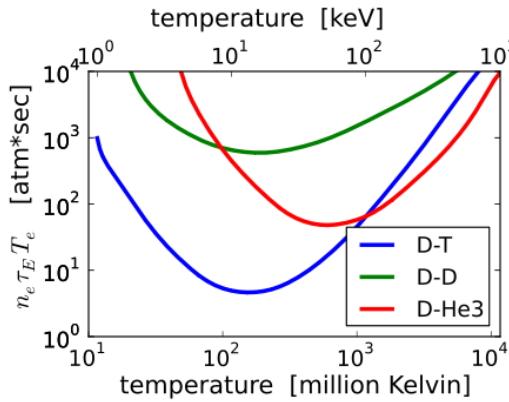


Figure 1.5.: Triple product as a function of temperature for the D-T, D-D , D-He3 reactions [13]

An important figure for the efficiency of the plasma reactor is the fusion energy gain G . This corresponds to the ratio of fusion power produced in a nuclear fusion reactor P_{fusion} to the heating power required to maintain the plasma in steady state P_{heat} .

$$G = \frac{P_{fusion}}{P_{heat}} \quad (1.11)$$

The goal of ignition corresponds to a plasma which can heat itself by fusion energy without any external input, and can be described by $P_{heat} = 0$, namely by $G \rightarrow \infty$. Ignition is not a necessary condition for a practical reactor but

a value of G bigger than 5 is necessary since it means that the fusion heating power is greater than the external heating power [39].

1.2.2. Fusion Confinement

The most widely studied configuration for terrestrial fusion is based on the concept of magnetic confinement. The main representative of this concept are tokamaks, devices in the shape of a torus, which use electromagnets in order to confine the plasma. The stable plasma equilibrium is achieved with magnetic field lines that move around the torus in a helical shape. Such a helical pattern is obtained by the superposition of a toroidal field (created by superconducting coils surrounding the torus) and a poloidal field orthogonal to it (resulting from the ion flow in the plasma). Since the 1950s [31], when the idea of tokamaks was introduced into the scientific community, a lot of research has been invested into the development and improvement of its experimental setup, leading to an exponential increase of the fusion triple product [18] over the years, analog to Moore's law [16]. This effect is demonstrated in Fig. 1.6.

An example of a tokamak engine is the ASDEX Upgrade located at the Max Planck Institute of Plasma Physics in Garching which is illustrated in Fig. 1.7 [19].

The second advanced method of fusion confinement is the Inertial Confinement Fusion (ICF). In this concept, the fuel is compressed into a pellet, which is then irradiated with highly energetic laser light, electron or ion beams. Upon contact with the incoming beam, the inner core is increased a thousandfold in density and its temperature is driven upward to the ignition point for fusion [28].

As can be observed in Fig. 1.8, this process can be qualitatively split into four sections. At first, the incoming energy flux evaporates the outer layer of the pellet, producing energetic collisions which drive part of the pellet inward, while the heated outer layer explodes outward. The inward moving wave leads to a compression of the remainder of the target. A sufficiently powerful set of shock waves can compress and heat the fuel at the center so much that fusion reactions occur. The energy released by these reactions is capable of heating the surrounding fuel causing it to undergo fusion as well. The process reaches "ignition" when a chain reaction propagates through the biggest part of the fuel pellet. Due to the small timescale of the process (0.01 – 1ns), the ions do not move appreciably because of their own inertia; hence the name inertial

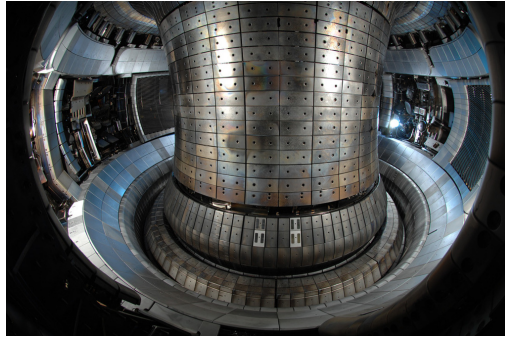


Figure 1.7.: Inside view of the ASDEX Upgrade Tokamak at the Max Planck Institute of Plasma Physics in Garching (Image from www.ipp.mpg.de)

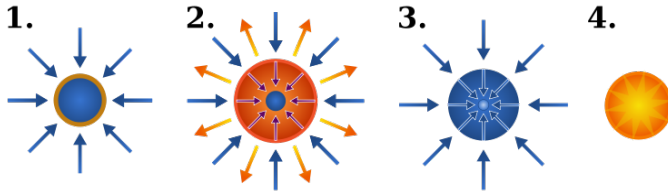


Figure 1.8.: Mechanism of Inertial Confinement Fusion

1.2.3. Fusion Propulsion Considerations

Despite the fact that gains close to 10 are projected by the beginning of the 2020 [14] decade during the operation of the ITER tokamak [16], the big masses associated with the magnetic confinement devices lead to low thrust to weight ratios. The main alternative to magnetic confinement is ICF, such as that proposed by Project Daedalus and Project ICARUS [1], [23]. A small pellet of fusion fuel (with a diameter of a couple of millimeters) would be ignited by an electron beam or a laser. Unlike Project Orion (where a pusher plate absorbs the kinetic energy of the fusion products) [11], to produce direct thrust a magnetic field would direct the created ions towards the outlet, thereby imparting

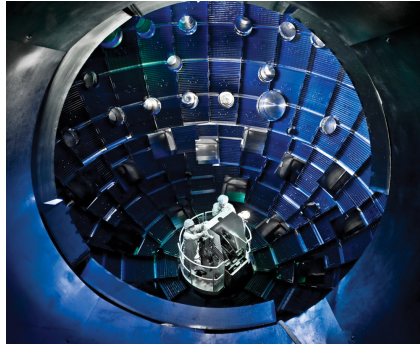


Figure 1.9.: The inside of the ignition chamber at the National Ignition Facility (Image from www.extremetech.com)

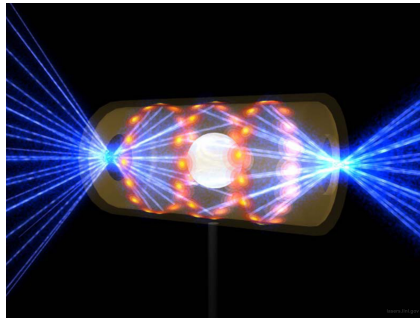


Figure 1.10.: Animation of the indirect ICF method using a Hohlraum (Image from www.llnl.gov)

part of their impulse on the spacecraft structure. In the 1980s, Lawrence Livermore National Laboratory and NASA studied an ICF-powered "Vehicle for Interplanetary Transport Applications" (VISTA). The conical VISTA spacecraft could deliver a 100-ton payload to Mars orbit and return to Earth in 130 days, or to Jupiter orbit and back in 403 days. Its operating principle is based on the fusion of deuterium/tritium (D-T).

1.2.4. Magnetic Nozzle

One of the most important characteristics of the ICF propulsion concept lies in the design of the magnetic nozzle system, which ensures the production of direct thrust. The idea of using magnetic fields for thrust application in fusion rockets was first introduced by R. A. Hyde [15]. The configuration of the coils ensures that the plasma flow, channeled by the diverging magnetic lines, expands supersonically in a similar way to a hot gas in a solid nozzle [4]. This operating principle is illustrated in Fig. 1.11 .

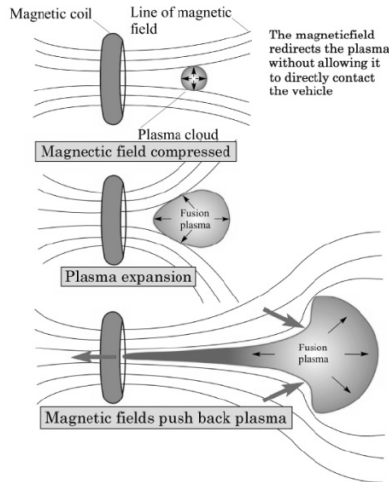


Figure 1.11.: Operating principle of magnetic nozzle [30]

The efficiency of a magnetic nozzle, η_{nozzle} , is defined as the fraction of the ion impulse that departs the nozzle in the desired direction compared to the total plasma impulse. Assuming a desired thrust direction along the x-axis, then the nozzle efficiency becomes:

$$\eta_{nozzle} = \frac{\int \rho v_x dV}{\int \rho |v| dV} \quad (1.12)$$

In Eq. 1.12, ρ stands for the density of the plasma, v_x for the velocity along the x direction and $|v|$ for the magnitude of the velocity, while the integration takes place over the volume V .

Several approaches have been taken for the calculation of the nozzle efficiency and the plasma flow inside the magnetic nozzle after ignition. R. A. Hyde based his work on a 2D Magnetohydrodynamics (MHD) code, which produced values close to 65 % for the thrust efficiency in a single coil nozzle. In their works, Nagamine et al. [27] and Kawasaki et al. [35] combined MHD with a Cubic Interpolation Pseudoparticle (CIP) scheme, and produced time dependent results for the nozzle efficiency.

Kawabuchi [30] and Vchivkov [37] relied on a Particle in Cell Method to calculate the plasma flow for different coil configurations. Matsuda et al. [25] provided values close to 78% for the nozzle efficiency, while using a Smoothed Particle Hydrodynamics (SPH) code [34]. Finally, different authors have simulated the plasma flow using hybrid methods. Nagamine [27] and Kajimura [26], [42] used 3D hybrid codes in order to simulate multiple coil configurations as well as to obtain efficiencies for thrust angle variation techniques.

In the present work, an ideal MHD approach is taken in order to simulate the behaviour of the plasma inside the magnetic nozzle. Although hybrid and Particle In Cell (PIC) codes have demonstrated useful results for a variety of nozzle geometries, it is considered interesting to observe whether some hydrodynamic effects are being ignored by these methods, which can still be captured using MHD. Since ideal MHD represents the simplest possible form of modeling (due to the fact that resistive and viscous terms are neglected), it is of interesting to observe what effects this simplification induces in the modeling of magnetic nozzle flows. For this purpose a comparison with the different techniques used in literature can be obtained, leading to the identification of the advantages and disadvantages related to ideal MHD. In order to reduce the computational effort, a two-dimensional (2D) approach was followed for the simulation of the plasma expansion.

2. Modeling and Numerics

2.1. Magnetohydrodynamics

Magnetohydrodynamics represents the study of the magnetic properties of electrically conducting fluids. The fundamental concept behind MHD is the coupling between a hydrodynamic flow and the presence of magnetic fields. External fields can induce currents in a moving conductive fluid, which in turn polarizes the fluid and reciprocally changes the magnetic field itself. The set of equations that describe MHD are a combination of the Navier-Stokes equations of fluid dynamics and Maxwell's equations of electromagnetism.

We will restrict ourselves to the ideal MHD equations, which represent the simplest form of MHD. Ideal MHD assumes that the fluid has so little resistivity that it can be treated as a perfect conductor. In addition to the perfect conductivity, the analogy to the inviscid flow in fluid dynamics (Euler equations) applies in the case of ideal MHD, leading to the absence of viscous fluxes.

In order for the ideal MHD to hold, several conditions have to be met for the plasma system. The plasma has to be strongly collisional, so that the time scale of collisions is shorter than the other characteristic times in the system. This leads to the particle distributions being close to Maxwellian. The resistivity induced by these collisions has to be small and specifically the typical magnetic diffusion durations present in the system must be longer than any time scale of interest. This way effects like the Landau damping can be neglected [6]. Finally, the results should be viewed with focus on macroscopic length scales compared to the ion skin depth and the Larmor radius.

The conservation form of the ideal MHD equations can be written as

$$\frac{\partial}{\partial t} U + \nabla \cdot \mathbf{F}^a(U) = S \quad (2.1)$$

with the advection flux \mathbf{F}^a and the vector of conserved variables

$$U = \begin{pmatrix} \rho \\ \rho \mathbf{v} \\ \tilde{\mathcal{E}} \\ \mathbf{B} \end{pmatrix} = (\rho, \rho v_1, \rho v_2, \rho v_3, \tilde{\mathcal{E}}, B_1, B_2, B_3)^T. \quad (2.2)$$

The term $\mathbf{v} = (v_1, v_2, v_3)^T$ stands for the fluid velocity, whereas $\mathbf{B} = (B_1, B_2, B_3)^T$ represents the magnetic field strength. $\tilde{\mathcal{E}}$ is the total volume specific energy of the fluid. This comprises of three different terms, the thermodynamic energy \mathcal{E}_T , the kinetic energy \mathcal{E}_K and the magnetic energy \mathcal{E}_M .

$$\tilde{\mathcal{E}} = \mathcal{E}_T + \mathcal{E}_K + \mathcal{E}_M = \frac{p}{\gamma - 1} + \frac{1}{2} \rho |\mathbf{v}|^2 + \frac{1}{2} \frac{|\mathbf{B}|^2}{\mu_0} \quad (2.3)$$

γ is the heat capacity ratio (Poisson's constant), μ_0 the magnetic permeability constant equal to $4\pi \frac{\text{H}}{\text{m}}$ and p the thermodynamic pressure of the fluid. The sum of thermodynamic and magnetic pressure is given by

$$\tilde{p} = p + \frac{1}{2} \frac{|\mathbf{B}|^2}{\mu_0} \quad (2.4)$$

In the case where external sources are ignored ($S = 0$), the full equation system [17] reads as :

$$\frac{\partial}{\partial t} \rho = -\nabla \cdot (\rho \mathbf{v}), \quad (2.5)$$

$$\frac{\partial}{\partial t} (\rho \mathbf{v}) = -\nabla \cdot \left(\rho \mathbf{v} \mathbf{v}^T + \tilde{p} \underline{\mathbf{I}} - \frac{1}{\mu_0} \mathbf{B} \mathbf{B}^T \right), \quad (2.6)$$

$$\frac{\partial}{\partial t} \tilde{\mathcal{E}} = -\nabla \cdot \left(\left(\tilde{\mathcal{E}} + \tilde{p} \right) \mathbf{v} - \frac{1}{\mu_0} \mathbf{B} (\mathbf{B} \cdot \mathbf{v}) + \frac{1}{\mu_0^2} ((\nabla \times \mathbf{B}) \times \mathbf{B}) \right), \quad (2.7)$$

$$\frac{\partial}{\partial t} \mathbf{B} = -\nabla \cdot \left(\mathbf{v} \mathbf{B}^T - \mathbf{B} \mathbf{v}^T \right). \quad (2.8)$$

together with the divergence constraint

$$\nabla \cdot \mathbf{B} = 0. \quad (2.9)$$

The identity tensor is given by $\underline{\mathbf{I}}$. It is important to point out that the third term in the impulse equation, $\nabla \cdot \left(\frac{1}{\mu_0} \mathbf{B} \mathbf{B}^T \right)$ results from the Lorentz force due to the interaction of the current density \mathbf{j} and the magnetic field \mathbf{B}

$$\mathbf{j} \times \mathbf{B} = \frac{(\nabla \times \mathbf{B})}{\mu_0} \times \mathbf{B}. \quad (2.10)$$

The advection flux becomes:

$$\mathbf{F}^a = \begin{pmatrix} \rho \mathbf{v} \mathbf{v}^T + \tilde{p} \underline{\mathbf{I}} - \frac{1}{\mu_0} \mathbf{B} \mathbf{B}^T \\ (\tilde{\mathcal{E}} + \tilde{p}) \mathbf{v} - \frac{1}{\mu_0} \mathbf{B} (\mathbf{B} \cdot \mathbf{v}) \\ \mathbf{v} \mathbf{B}^T - \mathbf{B} \mathbf{v}^T \end{pmatrix}. \quad (2.11)$$

2.1.1. MHD with external field

In the formulation described in Eq. 2.8, the total magnetic field in the plasma is defined as time dependent and can undergo changes due to the induction of internal fields due to the plasma movement. However, in the case of a magnetic nozzle, the field created by the magnetic coils remains constant over time and does not alter depending on the fluid induced field. For that reason, a separation is required between the constant, external (background) field \mathbf{B}_0 and the flow induced field \mathbf{B}_{in} . We follow the decomposition in [9] of the total magnetic field \mathbf{B} , in order to avoid numerical or physical damping of the strong background field reads as:

$$\mathbf{B} = \mathbf{B}_0 + \mathbf{B}_{in} \quad (2.12)$$

where $\frac{\partial}{\partial t} \mathbf{B}_0 = \mathbf{0}$ and $\nabla \cdot \mathbf{B}_0 = 0$. Apart from the magnetic field, a change in the update of the fluid energy is introduced. Instead of computing the time derivative of the total energy as in Eq. 2.7, the total perturbation energy $\tilde{\mathcal{E}}_{in}$ is calculated as:

$$\tilde{\mathcal{E}}_{in} = \frac{p}{\gamma - 1} + \frac{1}{2} \rho |\mathbf{v}|^2 + \frac{1}{2} \frac{|\mathbf{B}_{in}|^2}{\mu_0} = \tilde{\mathcal{E}} - \frac{1}{\mu_0} \left(\frac{1}{2} |\mathbf{B}_0|^2 + \mathbf{B}_0 \cdot \mathbf{B}_{in} \right) \quad (2.13)$$

In a similar manner, the total perturbation pressure \tilde{p}_{in} is given by:

$$\tilde{p}_{in} = p + \frac{1}{2} \frac{|\mathbf{B}_{in}|^2}{\mu_0} \quad (2.14)$$

Therefore, the conservation variables U are modified to

$$U = \begin{pmatrix} \rho \\ \rho \mathbf{v} \\ \tilde{\mathcal{E}}_{in} \\ \mathbf{B}_{in} \end{pmatrix}, \quad (2.15)$$

whereas the advection flux \mathbf{F}^a is given by Eq. 2.16 [9].

$$\mathbf{F}^a = \begin{pmatrix} \rho \mathbf{v} \\ \rho \mathbf{v} \mathbf{v}^T + \tilde{p} \underline{\mathbf{I}} - \frac{1}{\mu_0} \mathbf{B} \mathbf{B}^T - \frac{1}{\mu_0} \left(\frac{1}{2} |\mathbf{B}_0|^2 \underline{\mathbf{I}} - \mathbf{B}_0 \mathbf{B}_0^T \right) \\ \left(\tilde{\mathcal{E}}_{in} + \tilde{p}_{in} \right) \mathbf{v} - \frac{1}{\mu_0} \left(\mathbf{B} (\mathbf{B}_1 \cdot \mathbf{v}) - \mathbf{v} (\mathbf{B}_0 \cdot \mathbf{B}_1) \right) \\ \mathbf{v} \mathbf{B}^T - \mathbf{B} \mathbf{v}^T \end{pmatrix}. \quad (2.16)$$

Apart from this hyperbolic flux, an additional source term is added to the energy equation and reads as

$$S = \frac{1}{\mu_0} (\mathbf{B} \times \mathbf{v}) \cdot (\nabla \times \mathbf{B}_0) \quad (2.17)$$

However, in the case of stationary external fields like the ones examined in this work, the rotation of \mathbf{B}_0 remains equal to zero ($\nabla \times \mathbf{B}_0 = 0$) and therefore, this source term will not be included.

2.1.2. Waves in MHD

MHD is a fluid theory and there are similar wave modes as in ordinary fluid theory (hydrodynamics). In hydrodynamics the restoring forces for perturbations are the pressure gradient and gravity. Also in MHD the pressure force leads to acoustic fluctuations, whereas Lorentz's force leads to a new class of wave modes, called Alfvén (or MHD) waves [6]. Due to the basic assumption of MHD that changes of electric field \mathbf{E} are slow, leading to $\partial \mathbf{E} / \partial t \approx 0$, the displacement current is neglected in the Ampere-Maxwell law and MHD is incapable of describing electromagnetic waves. Therefore, the MHD waves have no direct connection to electromagnetic waves through the plasma.

The simplest wave mode propagating in a fluid is the sound wave, which travels with the speed

$$v_S = \sqrt{\frac{\gamma p}{\rho}} \quad (2.18)$$

through a medium with pressure p and density ρ . The sound wave is a propagating pressure perturbation whose wave vector \mathbf{k} is normal to the pressure front.

For an intuitive understanding of the MHD waves, the nature of the Lorentz force has to be examined. This force can be split into two components as shown in [6], resulting to

$$\mathbf{j} \times \mathbf{B} = (\mathbf{B} \cdot \nabla) \frac{\mathbf{B}}{\mu_0} - \nabla \left(\frac{\mathbf{B}^2}{2\mu_0} \right) \quad (2.19)$$

The second term in Eq. 2.19 acts on the fluid in the same way as the pressure force $-\nabla p$ and for that reason $\frac{\mathbf{B}^2}{2\mu_0}$ is called that magnetic pressure. The first term can be written as

$$(\mathbf{B} \cdot \nabla) \frac{\mathbf{B}}{\mu_0} = \frac{\partial}{\partial s} \left(\frac{\mathbf{B}^2}{2\mu_0} \right) \mathbf{e}_t - \frac{\mathbf{B}^2}{\mu_0 R} \mathbf{e}_n \quad (2.20)$$

Here s is now a coordinate measured along a magnetic field line, \mathbf{e}_t and \mathbf{e}_n are unit vectors in the tangential and principal normal direction, respectively, and R is the local radius of curvature of the field line.

Considering a flux tube as shown in Fig. 2.1, the force $(\mathbf{B} \cdot \nabla) \frac{\mathbf{B}}{\mu_0}$ can be interpreted as an effect produced by tensile stresses $\frac{\mathbf{B}^2}{\mu_0}$ acting on the ends of the tube. The force can be then split into two components demonstrating that the field lines are being in tension and exerting a pseudo-elastic stress on the fluid.

As described in [33] the MHD equations for impulse, mass continuity and magnetic field lead to the existence of wave traveling through the conducting plasma, leading to an oscillatory movement of its ions. The general dispersion equation for plane waves of the form

$$\mathbf{v}_1(\mathbf{r}, t) = \mathbf{v}_1 \exp[i(\mathbf{k} \cdot \mathbf{r} - \omega t)] \quad (2.21)$$

with angular frequency ω is given by

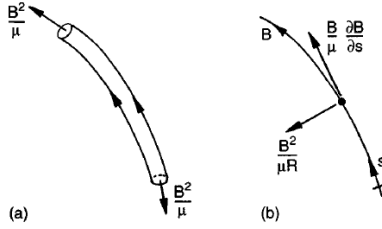


Figure 2.1.: Magnetic tension forces along a field line [6]

$$-\omega^2 \mathbf{v}_1 + (v_A^2 + v_S^2)(\mathbf{k}^T \mathbf{v}_1) \mathbf{k} + (\mathbf{k}^T \mathbf{v}_A) \left[(\mathbf{k}^T \mathbf{v}_A) \mathbf{v}_1 - (\mathbf{v}_1^T \mathbf{v}_A) \mathbf{k} - (\mathbf{k}^T \mathbf{v}_1) \mathbf{v}_A \right] = 0 \quad (2.22)$$

\mathbf{v}_A is defined as the vector of the Alfvén velocity with direction towards the external magnetic field and magnitude equal to v_A .

$$v_A = \sqrt{\frac{B^2}{\rho \mu_0}} \quad (2.23)$$

The Alfvén speed is a characteristic property in the MHD and represents the ratio of the stress tension to the mass density as shown in Eq. 2.23.

For a propagation of the wave in an arbitrary angle θ with respect to \mathbf{v}_A and hence to the magnetic field, three different wave modes can occur: 1) the pure Alfvén wave 2) the slow MHD wave 3) the fast MHD wave

The phase velocities as a function of the angle θ read out as:

$$v_{\phi, Alfvén} = v_A \cos \theta \quad (2.24)$$

$$v_{\phi, slow}^2 = \frac{1}{2}(v_A^2 + v_S^2) - \frac{1}{2} \sqrt{(v_A^2 + v_S^2)^2 - 4v_S^2 v_A^2 \cos^2 \theta} \quad (2.25)$$

$$v_{\phi, fast}^2 = \frac{1}{2}(v_A^2 + v_S^2) + \frac{1}{2} \sqrt{(v_A^2 + v_S^2)^2 - 4v_S^2 v_A^2 \cos^2 \theta} \quad (2.26)$$

All these waves have constant phase velocities for all frequencies, and hence there is no dispersion. At the limits when the angle between the wave propagation vector \mathbf{k} and magnetic field \mathbf{B} is either 0 or 90 degrees, the wave modes obtain the names and properties described in Table 2.1.

Table 2.1.: MHD waves

Name	Properties	Phase velocity v_ϕ
Sound wave	$\mathbf{k} \parallel \mathbf{v}_A$, $\mathbf{k} \parallel \mathbf{v}_1$	v_S
Alfven wave	$\mathbf{k} \parallel \mathbf{v}_A$, $\mathbf{k} \perp \mathbf{v}_1$	v_A
Magnetosonic wave	$\mathbf{k} \perp \mathbf{v}_A$, $\mathbf{k} \parallel \mathbf{v}_1$	v_M

Quantitatively, the restoring force for the Alfven wave propagation is the magnetic field tension. The existence of this wave mode is illustrated in Fig. 2.2. A velocity perturbation leads to a curvation of the magnetic field lines and hence to a restoring force which can surpass the inertia of the fluid and change its direction of motion. The produced disturbance can then move along the field line, leading to a wave oscillation with transversal nature.

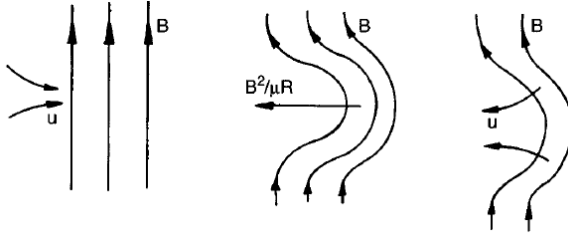


Figure 2.2.: Perturbation of magnetic field line and restoring force [6]

In the direction perpendicular to \mathbf{B} and the case of a magnetosonic wave, a longitudinal oscillation is made possible by the magnetic restoring force (magnetic pressure). The propagation of this wave involves compression and rarefaction of the magnetic lines as well as the plasma as illustrated in Fig. 2.3.

2. Modeling and Numerics

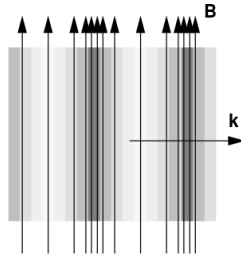


Figure 2.3.: (Image from www.theory.physics.helsinki.fi) Magnetosonic wave compressing and releasing the lines of force and the conducting fluid perpendicularly to \mathbf{B}

The propagation of this wave is given by

$$v_M = \sqrt{v_A^2 + v_s^2} \quad (2.27)$$

A schematic overview of the phase velocity $v_\phi = \omega/k$ as a function of the angle θ can be obtained in Fig. 2.4.

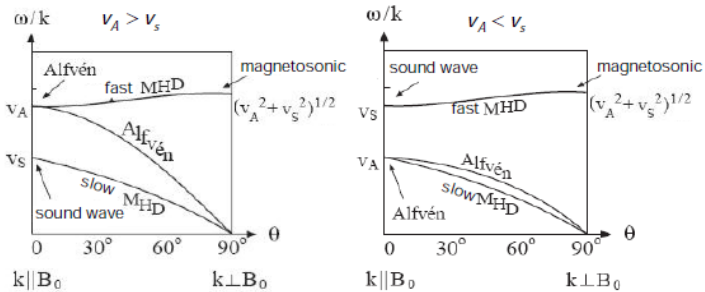


Figure 2.4.: Phase velocity as a function of the angle between wave vector and magnetic field vector (Image from www.theory.physics.helsinki.fi)

2.2. Finite Volume Methods

The solution of the MHD equations is implemented numerically, using a Finite Volume Method (FVM). The solver Flexi [12], initially developed at the Institute for Aerodynamics and Gas Dynamics (IAG) of the University Stuttgart was used during the present work.

Finite Volume Methods are used to represent and evaluate partial differential equations (PDEs) in the form of algebraic equations. Just like in all numerical schemes for the solution of PDEs, the values of the sought variables are calculated discretely on a discretized geometry. The starting point for the formulation of the FVM is the integral form of the conservation laws for the variable U .

According to Eq. 2.1, an integration of the conservation form over the volume V_i of a small cell leads to :

$$\int_{V_i} \frac{\partial}{\partial t} U dV + \int_{V_i} \nabla \cdot \mathbf{F}(U) dV = \int_{V_i} S dV \quad (2.28)$$

By integrating the first term to get the volume average \bar{U}_i and by making use of Gauss' divergence theorem on the second integral term, one obtains:

$$V_i \frac{d\bar{U}_i}{dt} + \oint_{A_i} \mathbf{F}(U) \mathbf{n} dA = \bar{S}_i V_i \quad (2.29)$$

or equivalently:

$$\frac{d\bar{U}_i}{dt} + \frac{1}{V_i} \oint_{A_i} \mathbf{F}(U) \mathbf{n} dA = \bar{S}_i \quad (2.30)$$

where A_i represents the total surface area of each cell, and \mathbf{n} the normal unit vector of the surface, directed outwards from the cell. The values for the edge fluxes can be reconstructed by interpolation or extrapolation of the cell averages. The idea of the FVM discretization and control volume consideration is illustrated in Fig. 2.5.

In order to analyze the time discretization of Eq. 2.30, a one dimensional simplification is carried out. Taking a cell at position x_i and edges at $x_{i-1/2}$ and $x_{i+1/2}$ and defining $\Delta x = x_{i+1/2} - x_{i-1/2}$ yields:

$$\frac{d\bar{U}(x_i, t)}{dt} + \frac{1}{\Delta x} [f(U(x_{i+1/2}, t)) - f(U(x_{i-1/2}, t))] = \bar{S}(x_i, t) \quad (2.31)$$

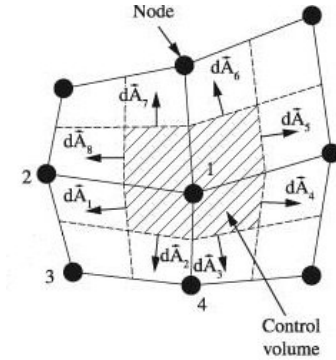


Figure 2.5.: Finite Volume Method (Image from www.scielo.br)

In Eq. 2.31, $f(U(x_{i+1/2}, t)) - f(U(x_{i-1/2}, t))$ is the difference between the incoming and outgoing integrated fluxes through the edges of the control cell. By introducing the time step n and the spatial coordinates as indices:

$$\left(\frac{d\bar{U}}{dt} \right)_i^n + \frac{1}{\Delta x} (f_{i+1/2}^n - f_{i-1/2}^n) = \bar{S}_i^n \quad (2.32)$$

An illustration of this situation can be observed in Fig. 2.6.

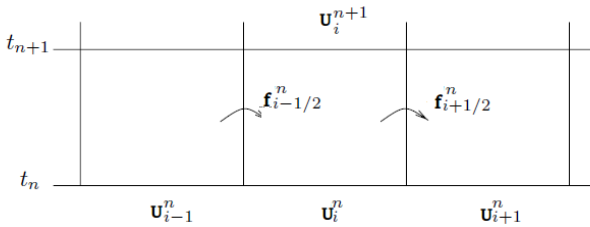


Figure 2.6.: Finite Volumes Method time scheme

For the solution of the Ordinary Differential Equation (ODE) shown in Eq. 2.32 a Runge Kutta method of 3rd order was used.

Moreover the Lax-Friedrichs (LF) flux is utilized for the solution of the resulting Riemann problem [36], [22]. According to the general principle of a Riemann solver, the evaluation of the integrated fluxes $f(U(x_{i+1/2}, t))$ and $f(U(x_{i-1/2}, t))$ is a function g of the conservative variables U_i , U_{i+1} and U_{i-1} .

$$f(U(x_{i\pm 1/2}, t)) = g(U_i, U_{i\pm 1}, t) \quad (2.33)$$

In the case of the LF method, this calculation takes the form in Eq. 2.34 and Eq. 2.35 when a first order scheme is used.

$$f(U(x_{i+1/2}, t)) = \frac{1}{2} (f(U_i, t) + f(U_{i+1}, t)) - \lambda_{max}(U_i - U_{i+1}) \quad (2.34)$$

$$f(U(x_{i-1/2}, t)) = \frac{1}{2} (f(U_i, t) + f(U_{i-1}, t)) - \lambda_{max}(U_{i-1} - U_i) \quad (2.35)$$

In this notation, λ_{max} represents the highest wave speed resulting from the states U_{i-1} and U_i .

In this work, the first order FVM was employed, for stability and robustness reasons, since strong shock fronts are part of the solution.

3. Initialization

3.1. Conditions after Ignition

In the ICF concept, the confined fuel must reach high temperatures and densities to produce enough thermonuclear reactions, so that the total energy released by the fusion reactions is much greater than the driver energy required to compress the fuel. In the current direct-driven ICF applications, a cryogenic deuterium and tritium spherical capsule filled with DT gas is accelerated inward by direct laser irradiation [43]. In order to compress the fuel to the desired temperature and density, the laser pulse starts by driving a shock through the shell. As the shock propagates inside the shell, the laser power begins to rise and subsequently launches a compression wave traveling inward. When the shock and compression wave merge and break out on the inner shell surface, an outward traveling rarefaction wave is launched from this surface due to the density discontinuity at the shell and gas interface. Once the rarefaction wave breaks out, the shell outer surface senses the lower pressure and accelerates inward under the pressure of the laser driver. This marks the onset of the acceleration phase, during which the shell accelerates to a high implosion velocity. The acceleration phase ends when the laser is turned off and the shell starts traveling at an approximately constant implosion velocity.

The deceleration phase starts when the inward traveling shock reflects off the center of the capsule, hits the incoming inner shell surface, and the shell velocity slows down. The low-density gas enclosed by the inner shell surface develops a fairly uniform pressure and becomes part of the hot spot. At this point, the imploding shell acts like a spherical piston on the hot spot until it finally reaches stagnation. The hotspot pressure and temperature keep increasing as the shell kinetic energy is converted into internal energy through compression work. The hot-spot mass increases because the heat conducted from the hot spot to the shell causes more shell material to ablate off the shell inner surface into the hot spot. When the shell stagnates, the pressure is almost constant throughout the hot spot and the shell. Since the density is much larger in the shell than in the hot spot, the latter has much higher temperature. If the

3. Initialization

hot spot reaches the ignition conditions [5] deuterium-tritium DT reactions are self-sustained and generate a burn wave into the shell, thus igniting the main fuel.

Since the capsule performance depends on the stagnation parameters such as density, areal density and temperature, it is crucial to determine the relations between the in-flight and the stagnation variables, so that the target and laser pulse can be properly designed to meet the requirements for high performance implosions. A typical target configuration and laser power profile for the case of fast ignition [20] is shown in Fig. 3.1.

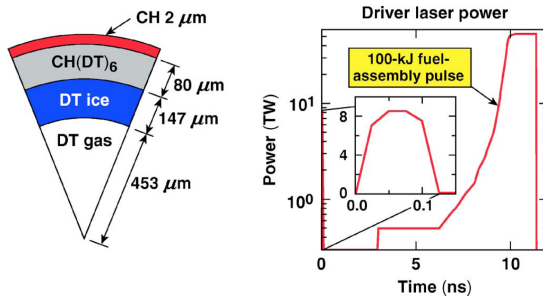


Figure 3.1.: Fusion Target and power profile for fast ignition ICF [43]

The hydrodynamic relations for direct-drive fast-ignition and conventional inertial confinement fusion explosion processes can be found in [43]. Typical profiles for the compressed target density and temperature are described in Fig. 3.2.

However, the modeling of such phenomena exceeds the purposes of the present thesis and therefore, no modeling of the ignition and initial implosion process was carried out. As described in detail in Section 3.2, a developed macroscopic state is chosen as the starting point of the modeling process. In ICF power reactors, the energy of the plasma resulting from the implosion of the target should be utilized for power production before it expands to larger dimensions. In fusion propulsion applications however, the plasma expands in the presence of a magnetic field to flow out of the magnetic nozzle, when detaching from the

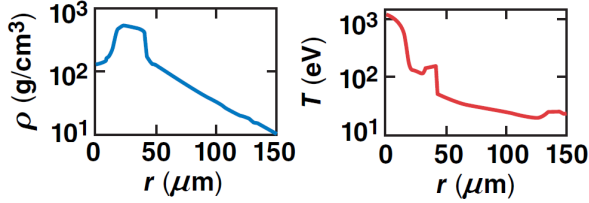


Figure 3.2.: Density and temperature profile along radius of pellet for fast ignition ICF [43]

magnetic field lines [3]. For that reason, an extended initial dimension of the plasma is possible for the current modeling.

3.2. Developed Initial Conditions

In an analog manner to previous works related to the efficiency of magnetic nozzles for fusion propulsion applications, initial conditions were examined, where the plasma has reached uniform conditions (homogeneous density, temperature) and macroscopic expansion lengths comparable to the size of the nozzle (order of magnitude of 10^{-1} m). It was observed, that independent research groups based their work on the same initial conditions. Specifically, in the works of Kajimura et al. [26], Nagamine et al. [27] and Vchivkov et al. [37], three dimensional hybrid PIC codes were utilized with the same initial conditions.

The initial plasma radius was set to $r_p = 0.3$ m and its total mass to $m = 110$ mg. Further physical characteristics of the plasma were the atomic mass $A = 197$ u, the atomic number $Z = 79$ and the effective charge $q = 16.81$ e of the ions. The parameter concealing the initial ion velocities was given by the total energy of the plasma $E_{plasma} = 4$ MJ. The density and the temperature of the ions are defined equal to $\rho_{in} = 10^{-3}$ kg/m³ and $T = 100$ eV respectively. Finally, a single coil configuration was simulated, with a coil radius $R_c = 1$ m, coil current $I = 3.57$ MA and coil center at $x = -1$ m, with the plasma being located at the origin of the domain. The initialization parameters are given in Table 3.1.

Table 3.1.: Initial Conditions defined in [27]

Plasma energy	4 MJ
Plasma radius	0.3 m
Plasma mass	110 mg
Plasma density	10^{-3}kg/m^3
Ion temperature	100 eV
Ion atomic mass	197 u
Ion atomic number	79
Ion effective charge	16.81 e
Coil radius	1 m
Coil current	3.57 MA

3.2.1. Pressure of the plasma

The conditions described in Table 3.1 include implicit information regarding the pressure of the plasma. Specifically, using the information about the temperature and the density of the plasma, the mean pressure p can be obtained.

$$p = n k_B T = \rho \frac{R_{gas}}{M} T = 3.25 \cdot 10^4 \frac{N}{m^2} \quad (3.1)$$

where R_{gas} stands for the ideal gas constant, M for the molar mass of the gas and n for the particle density in m^{-3} .

3.2.2. Velocity of the plasma

The values provided in [27] include information only regarding the total energy of the plasma and do not explicitly mention the velocity of the ions. This information was extracted following an energy consideration. Specifically, since the thermodynamic conditions inside the plasma domain are known, the energy of the plasma connected to these thermodynamic properties, E_T , can be calculated according to

$$E_T = \frac{3}{2} N k_B T = m \frac{p}{(\gamma - 1) \rho} = 5.38 \text{kJ} \quad (3.2)$$

In Eq. 3.1, N represents the number of ions and γ the Poisson coefficient, equal to $5/3$ in the case of monoatomic ions. Comparing the thermodynamic component E_T to the total plasma energy E_{plasma} , it is evident that it represents only a small fraction of the total energy. Since the total energy of the plasma includes the kinetic (E_K) and the thermodynamic (E_T) components, the energy balance yields

$$E_K = E_{plasma} - E_T \approx E_{plasma} = 4\text{MJ} \quad (3.3)$$

This outcome is expected for a highly energetic plasma where the kinetic energies of the ions due to the energy released by the fusion reactions are dominant.

Since all particles comprising the plasma in the work of Nagamine et al. [27] are defined with the same properties (including velocity and atomic mass), the formulation of the total kinetic energy can be simplified in terms of the average ion velocity \bar{v} according to Eq. 3.4.

$$E_K = \sum_{i=1}^N \frac{1}{2} m_i v_i^2 = \sum_{i=1}^N \frac{1}{2} m_i \bar{v}^2 = \frac{1}{2} m \bar{v}^2 \quad (3.4)$$

This leads to $\bar{v} = 2.697 \cdot 10^5$ m/s. This velocity is defined radially outwards for the plasma ions and is applied uniformly within the plasma domain in the works presented in [27], [26] and [37].

3.3. Gas dynamic investigation of initialization uncertainty

The initial conditions described in the previous sections are used as guidelines for the initialization of the 2D MHD simulation. In order to be able to compare effectively between the present 2D MHD simulation and the past works, parameters like the volume specific kinetic energy have to remain unaltered. The goal of this consideration is not to reproduce the results of the previous works, but to examine the differences that another model (in this case ideal MHD) can induce, even when the starting conditions are similar. One parameter which cannot be modeled with ideal MHD is the charge of the ions. Since the formulation of MHD is based on a quasi-neutral plasma, the individual charge is not a free parameter like in the case of particle methods. Moreover, from the energy standpoint, due to the different domain dimensions (3D versus 2D), the total energy of the plasma is different, so the volume specific energy $\tilde{\mathcal{E}}$ has to

be equal. In the same energy consideration, it is important that the thermal energy of the plasma remains small compared to the kinetic one, similarly to the hybrid PIC case presented in Section 3.2. This way, the dominance of the kinetic terms will be evident and will be closer to the reality.

However, in the case of MHD, there are additional parameters that need to be modeled compared to PIC and hybrid methods. Specifically, the vacuum conditions outside of the energetic plasma domain require special treatment. Both the density and the pressure will have an influence on the expansion of the plasma and could lead to a non-negligible energy exchange between the energetic and the (initially) stationary particles. Specifically, the vacuum conditions should be modeled in such way, that the energy stored within the outside domain should be negligible compared to the kinetic energy of the energetic plasma. This way the effect of the surrounding particles can be ignored and the MHD case would resemble the initial conditions of Table 3.1.

3.3.1. Density of surrounding environment

An important parameter which is present in the MHD formulation of the problem, lies in the modeling of the density outside of the energetic plasma. Assuming that the magnetic nozzle is used as a part of the propulsion system in an interstellar mission, the density of the interstellar medium (close to $4 \cdot 10^{-22} \text{ kg/m}^3$ [29]) is present in the surrounding environment of the engine. The engine is operating in pulsed mode, meaning that ignitions take place in sequence with a high frequency (close to 50 Hz [1], eventually leading to remnant plasma in the nozzle from the previous ignition. The value of this density is negligible compared to the plasma one, but remains still several orders of magnitude above the Ultra High Vacuum (UHV) conditions of the interstellar environment.

In general, modeling a density discontinuity of multiple orders of magnitude between the plasma and the surrounding “vacuum” could lead to numerical instabilities. A strong discontinuity would lead to extreme shocks requiring fine meshes for their resolution. For that reason, a parametric study was carried out with the purpose of determining the biggest possible value of the outside density which could still serve as vacuum condition, when compared to the values of the plasma. A purely gas dynamic blast simulation was carried out for different values of the outside density in the absence of a magnetic field. For the initialization of the energetic plasma, a 2D section of a sphere (disc) with

3.3. Gas dynamic investigation of initialization uncertainty

radius $r_p = 0.3$ m was implemented, in order to retain the symmetry described in [27]. A detailed presentation of the disc initialization is given in Section 3.4.1. The density inside the disc area is fixed to $\rho_{in} = 10^{-3}$ kg/m³. A uniform velocity distribution was defined, with all energetic particles having a radially directed speed with the value $v_{in} = \bar{v} = 2.697 \cdot 10^5$ m/s. In order to focus only on the effects of the outside density, a constant pressure was initialized throughout the whole domain, equal to $3.25 \cdot 10^4$ N/m². A summary of the initial conditions is given in Table 3.2 .

To examine the effect of the outside density, the dimensions of the plasma blastwave were measured and compared for the different configurations after a constant physical time equal to $10 \mu\text{s}$. This length was defined as the radius at which the density of the plasma is equal to 90% of its maximal value. This choice is justified when examining the time durations considered in [27], where the results are shown for the first $8 \mu\text{s}$. The mesh used in the simulation is shown in Appendix C.

Table 3.2.: Initial conditions for the parametric study of outside density influence

Variable	Inside	Outside
Density	10^{-3} kg/m ³	ρ_{out}
Pressure	$3.25 \cdot 10^4$ N/m ²	$3.25 \cdot 10^4$ N/m ²
Velocity	$2.697 \cdot 10^5$ m/s	0 m/s
Magnetic field	0 T	0 T

The results of this study for different values of the density ratio ρ_{in}/ρ_{out} , can be obtained in Fig. 3.3.

As expected, a higher outside density (smaller ρ_{in}/ρ_{out} ratio) leads to an additional resistance against the expansion of the plasma and therefore to a smaller displacement within the same time interval. After exceeding a specific ratio between the initial densities inside and outside of the plasma domain, there is no additional change in the expansion size of the plasma, as one can observe in the saturation part of Fig. 3.3. In fact, the maximal expansion radius

3. Initialization

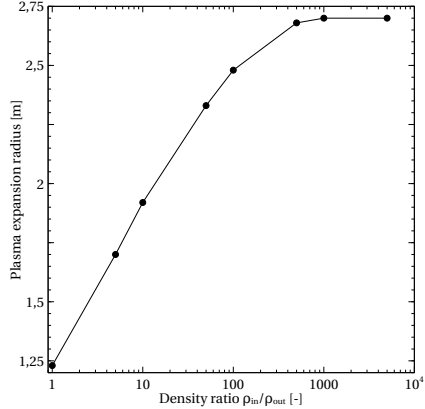


Figure 3.3.: Gas dynamic expansion at $t=10 \mu s$ for different density ratios ρ_{in}/ρ_{out}

measures close to 2.7 m and agrees with the theoretical distance that an undisturbed particle would travel through, when having a constant speed equal to $\bar{v} = 2.697 \cdot 10^5 \text{ m/s}$ for a duration of $10 \mu s$. The limit after which the effect of a further decrease in outer density becomes negligible, occurs at a factor of 1000, or explicitly for an outside density equal to $\rho_{out} = 10^{-6} \text{ kg/m}^3$. For that reason, this factor 1000 was defined as the condition of near vacuum in the domain outside of the plasma.

The importance of a low external density is obvious when taking into consideration the development of the total kinetic energy in the domain along time. The results of this investigation are shown in Fig. 3.4. Specifically, the kinetic energy of the plasma (normalized by its initial value for $t=0 \text{ s}$) is plotted against the physical time of the simulation in Fig. 3.4. The kinetic energy of the domain was defined as

$$E_K = \int \tilde{\mathcal{E}} dV = \int \frac{1}{2} \rho |\mathbf{v}|^2 dV \quad (3.5)$$

As expected due to the collisions between the highly energetic plasma particles and the (initially) stationary surrounding particles an impulse exchange takes

place, leading to a decrease in the kinetic energy. In the absence of an external field, the total energy is comprised of the sum of kinetic and thermodynamic energies, which implies that the kinetic energy “loss” is transformed into an increase in pressure (and hence thermodynamic energy). A higher value for the outside density leads to an increase of this phenomenon and to a bigger kinetic energy diffusion. For the density ratio chosen to represent the vacuum conditions (factor of 1000), the fraction of kinetic energy transformed into pressure increase, is limited to 10% during the first $10 \mu\text{s}$. This value was considered acceptable for the present analysis, since the effect of a further decrease in the external density in the kinetic energy profile was small.

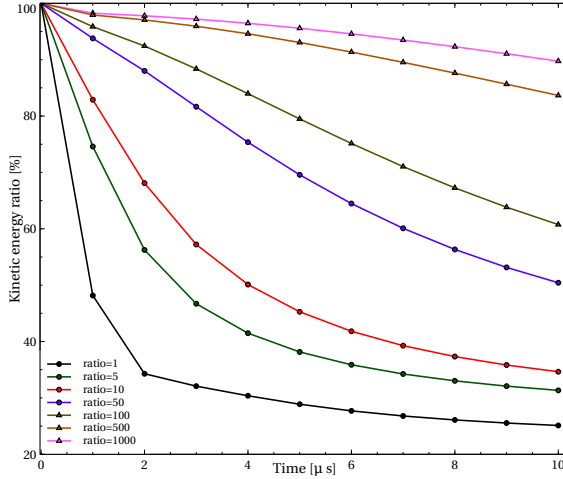


Figure 3.4.: Kinetic energy ratio (normalized to initial kinetic energy) along time for different density ratios ρ_{in}/ρ_{out}

3.3.2. Pressure of surrounding environment

Apart from the density of the environment, a further parameter requiring treatment (as opposed to the case of PIC and hybrid methods) is the pressure of the plasma and the surrounding environment. From the energy perspective, a pressure value would be needed, which would ensure that no severe influence

3. Initialization

on the total plasma energy takes place. The total energy per unit volume is obtained by the sum

$$\tilde{\mathcal{E}} = \frac{1}{2}\rho|\mathbf{v}|^2 + \frac{p}{\gamma - 1} \quad (3.6)$$

A low pressure in the vacuum is therefore needed in order to render the energy of the outside domain negligible. Nevertheless, the same consideration as in the case of the density is valid here, according to which a big discontinuity could lead to numerical instabilities. For that reason, a parametric analysis was carried out in order to examine the direct effect of the pressure ratio p_{in}/p_{out} . Following the same scheme as in the density variation, the pressure of the energetic plasma $p_{in} = 3.25 \cdot 10^4 \text{ N/m}^2$ remained constant, whereas the “vacuum” pressure p_{out} was altered. The initialization of the density followed the results of the previous section, with $\rho_{in} = 10^{-3} \text{ kg/m}^3$ and $\rho_{out} = 10^{-6} \text{ kg/m}^3$. The summarized plasma condition is shown in Table 3.3.

Table 3.3.: Initial Conditions for the parametric study of outside pressure influence

Variable	Inside	Outside
Density	10^{-3} kg/m^3	10^{-6} kg/m^3
Pressure	$3.25 \cdot 10^4 \text{ N/m}^2$	p_{out}
Velocity	$2.697 \cdot 10^5 \text{ m/s}$	0 m/s
Magnetic field	0 T	0 T

The results obtained for this variation of the outside pressure are shown in Fig. 3.5. Evidently, the effect of the pressure on the total kinetic energy is small due to the low vacuum density used (factor of 1000 smaller than the inside one), and reaches a saturation at a value of 50 for the ratio p_{in}/p_{out} . In order to model the physical condition of pressure difference between the energetic plasma and the vacuum, a factor of 100 was chosen for the pressure ratio, leading to $p_{out} = 3.25 \cdot 10^2 \text{ N/m}^2$.

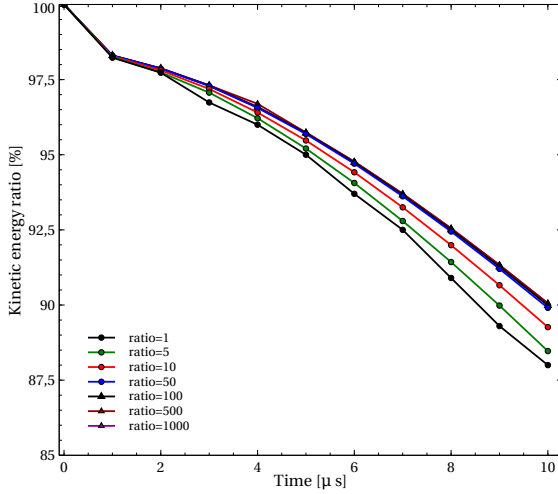


Figure 3.5.: Kinetic energy ratio (normalized to initial kinetic energy) along time for different pressure ratios p_{in}/p_{out}

3.4. Initial velocity profile

3.4.1. Uniform disc initialization

As presented in the discussion of the gas dynamic uncertainties, a possible initialization of the plasma conditions includes the definition of a disc domain, within which the properties are uniform. This approach was followed in the work of Nagamine et al [27], where the density and velocity of the plasma were initialized uniformly within a disc with radius $r_m = 0.3$ m, with a 2% perturbation of mode $m=50$, in order to smoothen out the discontinuity at the edge of the plasma. The resulting contour plot of the density for $t = 0 \mu\text{s}$ is presented in Fig. 3.6.

The area enclosed within the radius r_p has constant density and is therefore coloured uniformly (white). The dark annulus outside of this radius shows the contour lines due to the changing density, as the domain switches from the dense energetic plasma to the nearly empty vacuum domain. A radial plot of the plasma number density over the radius for $t = 1 \mu\text{s}$ is shown in Fig. 3.7.

3. Initialization

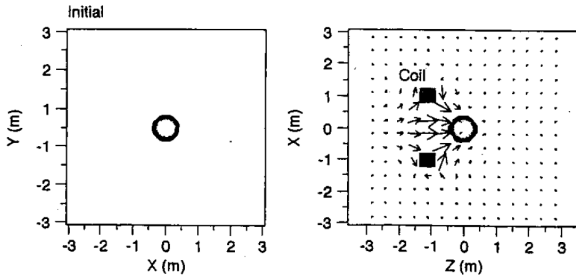


Figure 3.6.: Density contour plot during initialization [27]

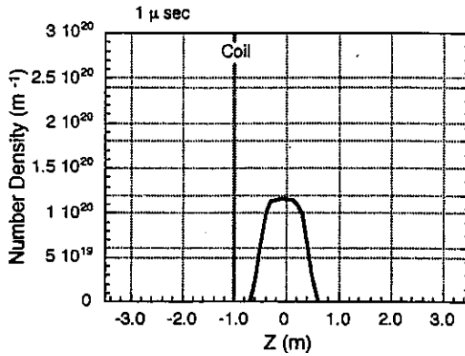


Figure 3.7.: Number density radial profile for $t = 1 \mu s$ [27]

The diffusion of the density at the edge has increased after $1 \mu s$, leading to a wider plasma domain of approximately 0.5 m.

In a similar process, the disc initialization of the 2D MHD simulation was performed with the values in Table 3.4. A visualisation of these profiles along the radial direction is shown in Fig. 3.8.

Table 3.4.: Initial Conditions for the uniform disc domain

Variable	Inside	Outside
Density	10^{-3} kg/m^3	10^{-6} kg/m^3
Pressure	$3.25 \cdot 10^4 \text{ N/m}^2$	$3.25 \cdot 10^2 \text{ N/m}^2$
Velocity	$2.697 \cdot 10^5 \text{ m/s}$	0 m/s
Magnetic field	0 T	0 T

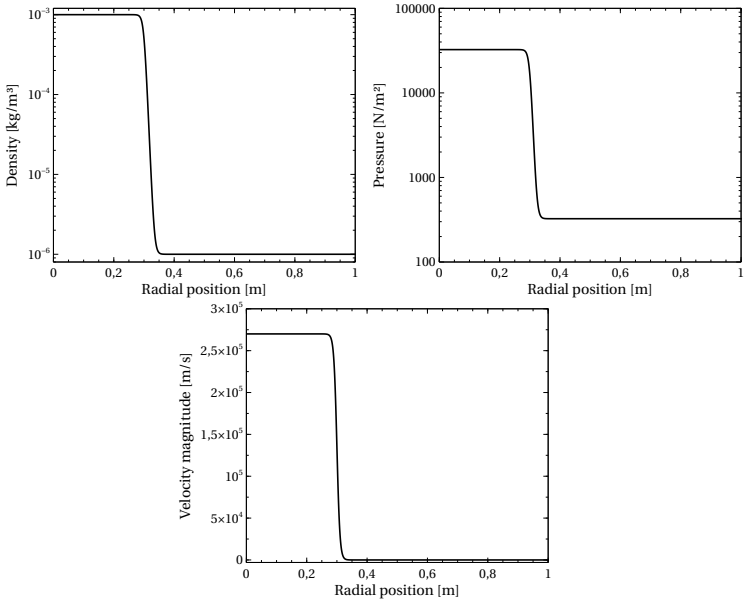


Figure 3.8.: Density, pressure and velocity profile for uniform disc initialization

With these initial conditions, the undisturbed expansion of the fluid in the absence of an external magnetic field was simulated. The results at $t = 0 \mu\text{s}$ and $t = 10 \mu\text{s}$ are shown in Fig. 3.9. One observes that due to the bigger ex-

3. Initialization

pansion of the plasma, its maximal density has decreased and reached values close to 50 times bigger than the modeled “vacuum” conditions. It is important that the smallest value of the density reaches 10^{-9} kg/m³. This occurs at the center of the domain and is a result of the radially outwards directed velocity vectors, which lead to a rarefaction of the inner region. This effect is further discussed in this section and in Appendix A. The pressure evolution is shown to demonstrate a thin annulus with high values which corresponds to the region of collisions between the expanding plasma ions with each other and with the vacuum fluid. This area is characterized by a higher volume specific thermodynamic energy. Again, values more than 1000 times smaller than the modeled vacuum ($\approx 1.2 \cdot 10^{-1}$ N/m²) are present in the center of the domain.

Finally a shock wave can also be observed which is expected due to the extremely high Mach number during initialization ($Ma \approx 37$) as one can observe in Fig. 3.10. Since the fluid exchange momentum, a velocity distribution is created, which leads to an increasing Mach number along the radius. However, due to the high value of the Mach number in this hypersonic flow, a sharp drop at the position of the normal shock takes place. The flow outside becomes subsonic again ($Ma < 1$).

From the standpoint of gas dynamics, the time evolution of this initial profile can lead to numerical issues at the center of the domain. Specifically, at this point the biggest discontinuity in the velocity component takes place. Taking as an example the x axis, a point infinitesimally to the right of the origin will have a positive velocity whereas a point on the left side will have a velocity in opposite direction but with the same magnitude. As described in Toro [36], an initialization with such a sharp discontinuity in the velocity components can lead to vacuum conditions at the origin. Effectively, the expansion of the gas due to the radially directed velocity component leads to a sharp drop in pressure and density. This phenomenon was verified with an 1D simulation where the initialization with a discontinuity in velocity was modeled. The results are illustrated in Appendix A and the effects resulting from this numerical issue are further analyzed in Section 4.1.

3.4.2. Linear profile disc initialization

Apart from the numerical issues triggered by the vacuum condition due to the velocity discontinuity, the disc initialization also predicts a less physically intuitive representation of the plasma expansion. After further consideration of

3.4. Initial velocity profile

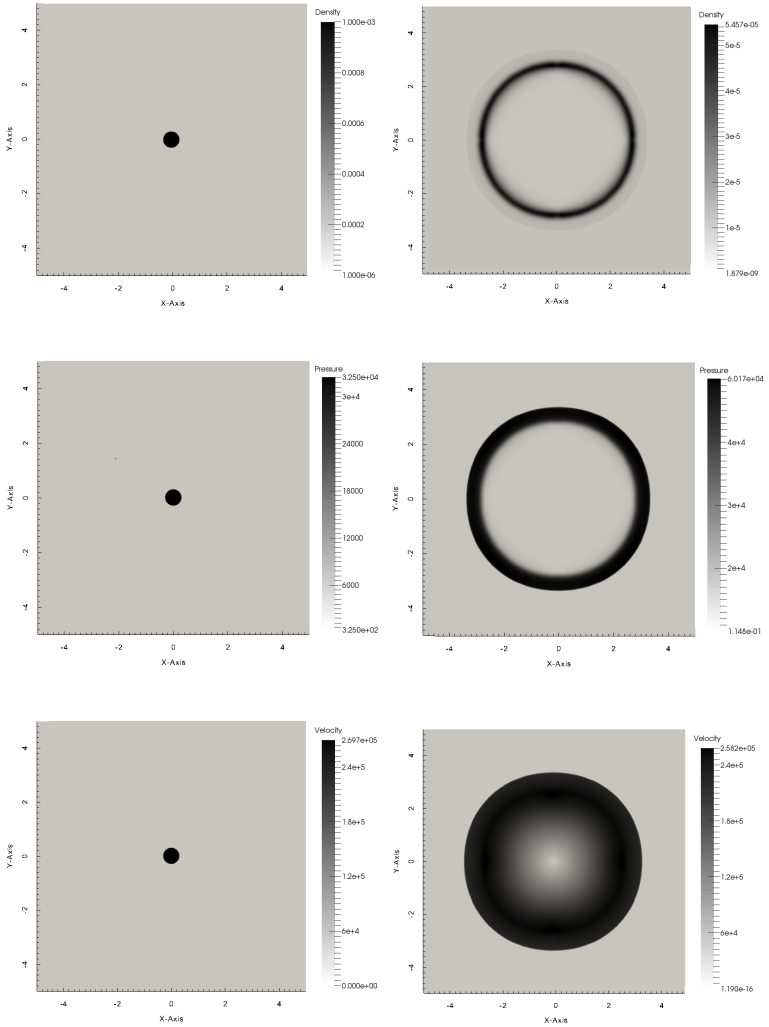


Figure 3.9.: Density, pressure and velocity distribution for the uniform disc initialization at $t = 0 \mu\text{s}$ (left) and $t = 10 \mu\text{s}$ (right)

3. Initialization

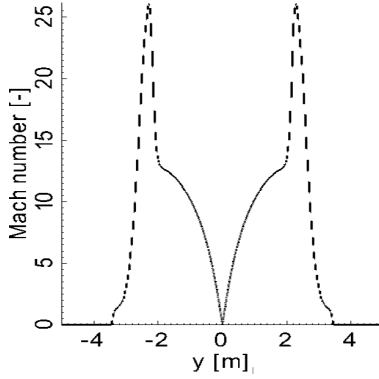


Figure 3.10.: Gas dynamic Mach number profile at $t = 10 \mu\text{s}$ for the uniform disc initialization

the initialization process, it was evident, that a uniform radial velocity could lead to an insufficient description of the plasma conditions, since particles located close to the center of the explosion are defined with the same velocity as the outer ones. At the moment defined as the starting point of the simulation, the plasma conditions have developed since the ignition, and therefore it is expected that all particles which have acquired a high speed have already moved further from the origin than the ones with smaller speeds. This leads to a velocity distribution with decreasing value for positions closer to the origin. For that reason, an initialization with linear velocity profile along the radial direction was analyzed. In this study, the density of the plasma was defined as uniform throughout the plasma domain.

Of course, such an assumption leads to a different value for the maximal speed of particles than the one shown in Table 3.4. The condition which was used in order to define the velocity of the plasma was based on the formulation of the kinetic energy. The total kinetic energy of the plasma should remain constant in order for a comparison between the two initializations to be valid. When a linear velocity distribution is assumed along the radius, the velocity profile takes the form

$$v(r) = v_{max} \cdot \frac{r}{r_p} \quad (3.7)$$

and the new kinetic energy becomes

$$E_{K,new} = \int_0^{r_p} \frac{1}{2} \rho(r) |\mathbf{v}(r)|^2 dV = \int_0^{r_p} \frac{1}{2} \rho_{in} \left(\frac{v_{max}}{r_p} r \right)^2 4\pi r^2 dr \quad (3.8)$$

For the energy equality to hold:

$$E_{K,new} = 4\text{MJ} \Rightarrow v_{max} = 3.433 \text{ m/s} \quad (3.9)$$

It was shown in Section 3.3.2 that the effect of the plasma pressure is not significant for the energy consideration. To avoid further numerical instabilities that could be caused by a varying pressure along the radius, the plasma pressure was defined as constant with the value $3.25 \cdot 10^4 \text{ N/m}^2$. A summary of the initial conditions is given in Table 3.5.

Table 3.5.: Initial Conditions for the linear profile domain initialization

Variable	Inside	Outside
Density	$\rho = 10^{-3} \text{ kg/m}^3$	$\rho = 10^{-6} \text{ kg/m}^3$
Pressure	$p = 3.25 \cdot 10^4 \text{ N/m}^2$	$p = 3.25 \cdot 10^2 \text{ N/m}^2$
Velocity	$v(r) = 3.433 \cdot 10^5 \text{ m/s} \cdot \frac{r}{0.3\text{m}}$	$v = 0 \text{ m/s}$
Magnetic field	$B = 0 \text{ T}$	$B = 0 \text{ T}$

The radial profiles of the initial conditions are visualised in Fig. 3.11.

3. Initialization

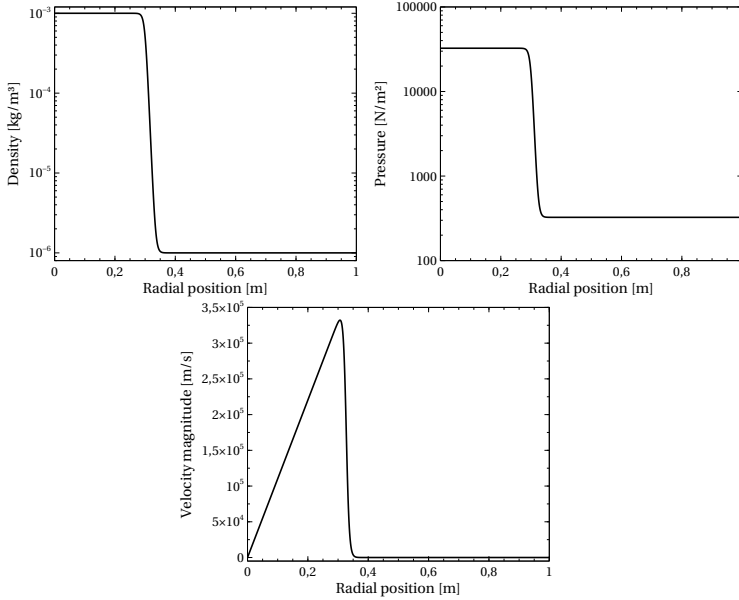


Figure 3.11.: Density, pressure and velocity profile for linear initialization

The forementioned initialization leads to the expansion properties described in Fig. 3.13. Comparing these results with the ones obtained by the uniform disc initialization, it is evident that the velocity and pressure distributions are very similar. The form of the 2D expansion and the maximal values for the particle speeds and plasma pressures are in the same range after $10 \mu\text{s}$ have elapsed. A difference observed lies in the value of the density and the dimensions of the plasma expansion at the end of simulation. A factor of 2 is present in the maximal density at $t = 10 \mu\text{s}$ ($5.45 \cdot 10^{-5} \text{ kg/m}^3$ for the uniform disc and $2.65 \cdot 10^{-5} \text{ kg/m}^3$ for the linear case). This is caused mainly due to the bigger maximum velocity in the linear profile initialization, which leads to a slightly bigger dimension of the blast and hence to a smaller density value.

Another important asset is the value of pressure and density close to the origin at $t = 10 \mu\text{s}$. Specifically, the density at small radii is no longer smaller than

the vacuum value as opposed to the uniform initialization. In a similar manner, the minimal pressure observed is approximately 2 orders of magnitude bigger than in the previous case, thereby suggesting a bigger numerical stability and avoidance of unnecessarily small pressures.

In this case, a shock is again present due to the hypersonic flow. The profile of the Mach number over radial position can be seen in Fig. 3.12. Comparing it to Fig. 3.10, one notices that the increase of the Mach number along the radius takes place in a more uniform way, without the presence of big gradients. This is due to the fact that particles at smaller radii have retained their velocity as opposed to the uniform velocity case, where all particles move equal distances and are therefore gathered in a small annulus after the $t = 10 \mu\text{s}$ have elapsed. The shock is again observed almost at the same position but the maximal value of the Mach number is slightly decreased, mainly due to the lower density. Both initializations were used for the simulations with magnetic field in Chapter 4.

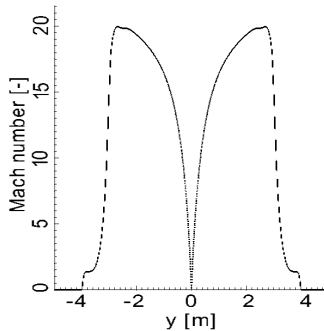


Figure 3.12.: Gas dynamic Mach number profile at $t = 10 \mu\text{s}$ (Linear Initialization)

3. Initialization

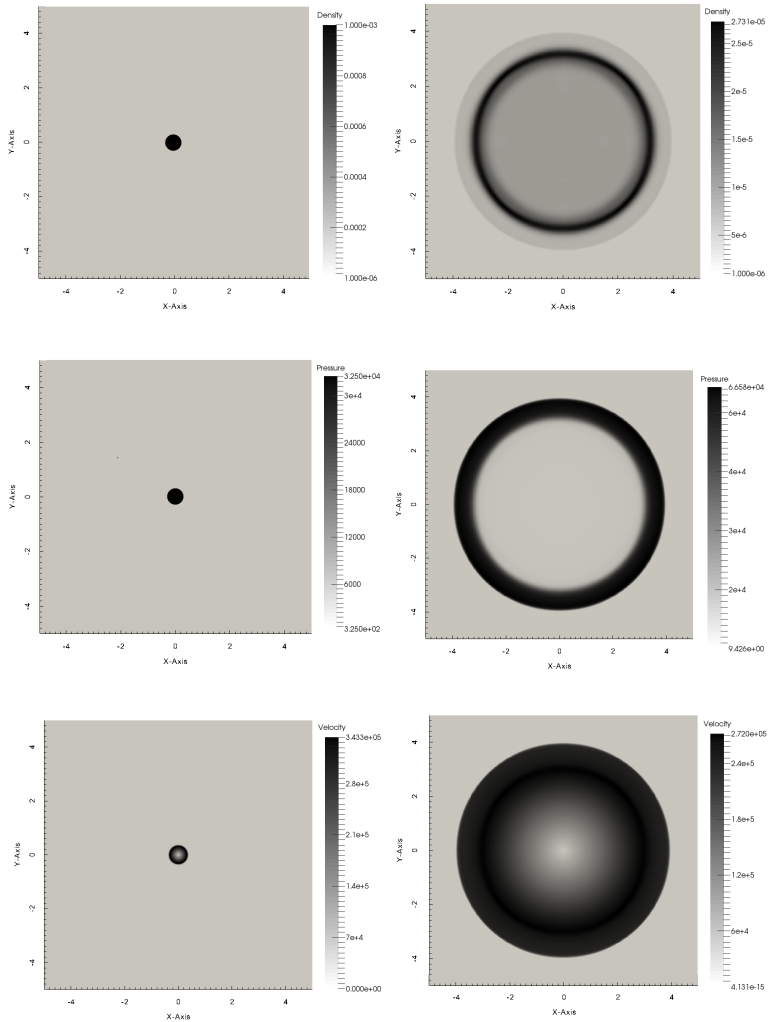


Figure 3.13.: Density, pressure and velocity distribution for the linear initialization at $t = 0 \mu\text{s}$ (left) and $t = 10 \mu\text{s}$ (right)

4. Results

4.1. Constant magnetic field

The concept of a magnetic nozzle involves the presence of external magnetic fields created by superconducting coils. In order to shape the plasma into a net thrust producing configuration, a non-uniform field has to be generated in the nozzle. However, in order to obtain an estimate of the interaction between the plasma and an external magnetic field in the ideal MHD case, simulations were performed where a time-independent, uniform external magnetic field was applied in the domain.

The interaction between the expanding plasma and the field was examined and compared for the two initializations described in Section 3.4. It was observed that an increasing magnetic field strength leads to numerical instabilities and specifically to pressure values very close to zero, which led to a crashing of the code.

4.1.1. Comparison of initializations

In order to examine the two initializations described in Section 3.4, the expansion of the plasma and its thermodynamic properties were observed under the influence of a constant magnetic field. Two different field strengths of $B = 0.05$ T and $B = 1$ T were used for comparison reasons and the direction of the field vector was kept constant along the x-axis.

In the case of the uniform disc initialization, both magnetic field strength resulted in a numerical instability, causing a negative pressure. In Fig. 4.1, the thermodynamic properties (density and pressure) as well as the value of the velocity in x direction are plotted along the x-axis. For each magnetic field strength, the initial values as well as the values at the final simulation time step (before the numerical instability) are shown. In the case of $B = 0.05$ T this occurs at $t = 0.55 \mu\text{s}$ and for $B = 1$ T at $t = 0.2 \mu\text{s}$.

4. Results

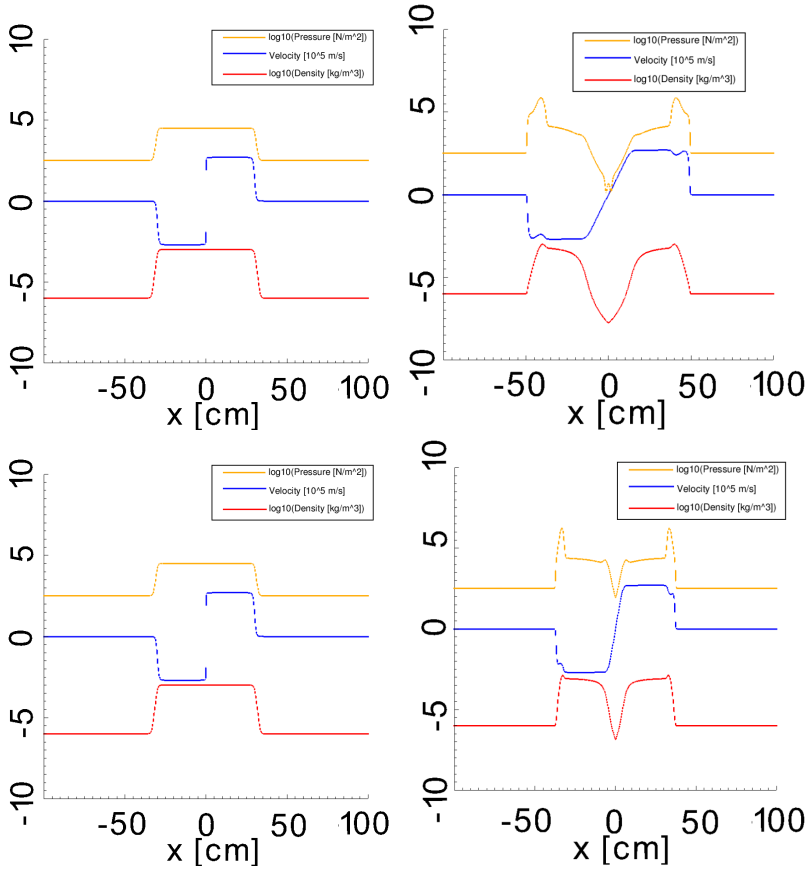


Figure 4.1.: Density, pressure and velocity along the x -axis for $t = 0 \mu\text{s}$ (left) and at the final time step (right) for $B = 0.05$ T (top) and $B = 1$ T (bottom) (uniform disc initialization)

For both magnetic field strength, the density and pressure acquire values several orders of magnitude smaller than vacuum. Due to the reasons explained in Section 3.4.1 and Appendix A, the high velocity gradient around the middle

point leads to a vacuum, which cannot be resolved by the code, thereby leading to negative values for the pressure and density. The general form of the profiles is equivalent for the two cases. Both demonstrate a shock close to the plasma edge (decrease in velocity and increase in pressure and density), which is expected for hypersonic speeds.

It can be observed however, that a stronger magnetic field leads to an earlier instability. This can be explained by the higher acceleration of the fluid particles. Another important factor that has to be considered is the presence of MHD waves. An increased field leads to a larger Alfvén speed and to a larger amplitude of the propagating wave. In the case of magnetosonic waves, where rarefactions in the pressure can be present, it is expected that an increased wave amplitude leads to a lower pressure. The characteristic wave speeds of the system are further analyzed in Section 4.1.3. Due to the small timescale of the simulation, the profiles of pressure, density and velocity along the y -direction do not differ from the ones along the x -axis and therefore the whole profile can be assumed as axis-symmetric.

In an analog manner, the same field strengths were used for the simulation of the case with linear initialization. For the 0.05 T case, no instability occurred during the simulation. The results at $t = 0 \mu\text{s}$ and $t = 1.2 \mu\text{s}$ are shown in Fig. 4.2. Results at future time steps ($t = 5 \mu\text{s}$ and $t = 10 \mu\text{s}$) can be found in Fig. 4.3.

One can observe that the decrease in pressure at the center is present but is put into action later. Eventually it also leads to the code crashing (negative pressure) but this occurs at approximately $t = 12.5 \mu\text{s}$ in this case. Due to the particles remaining closer to the origin and their smaller speeds, a smaller rarefaction near the origin takes place.

For the 1 T case, it was observed that the simulation encountered a numerical instability after $1.2 \mu\text{s}$. Upon examination of the pressure profile, it is obvious that the point of negative value is not longer located at the plasma origin but instead at the edge of the plasma front. Although a slight decrease in the pressure of the center is present, the effect is negligible compared to the “undershooting” at the location of the plasma edge, which leads to values smaller than the vacuum. The profile is shown in Fig. 4.2. A 2D contour plot of the pressure and velocity for $t = 1.2 \mu\text{s}$ can be seen in Fig. 4.4.

4. Results

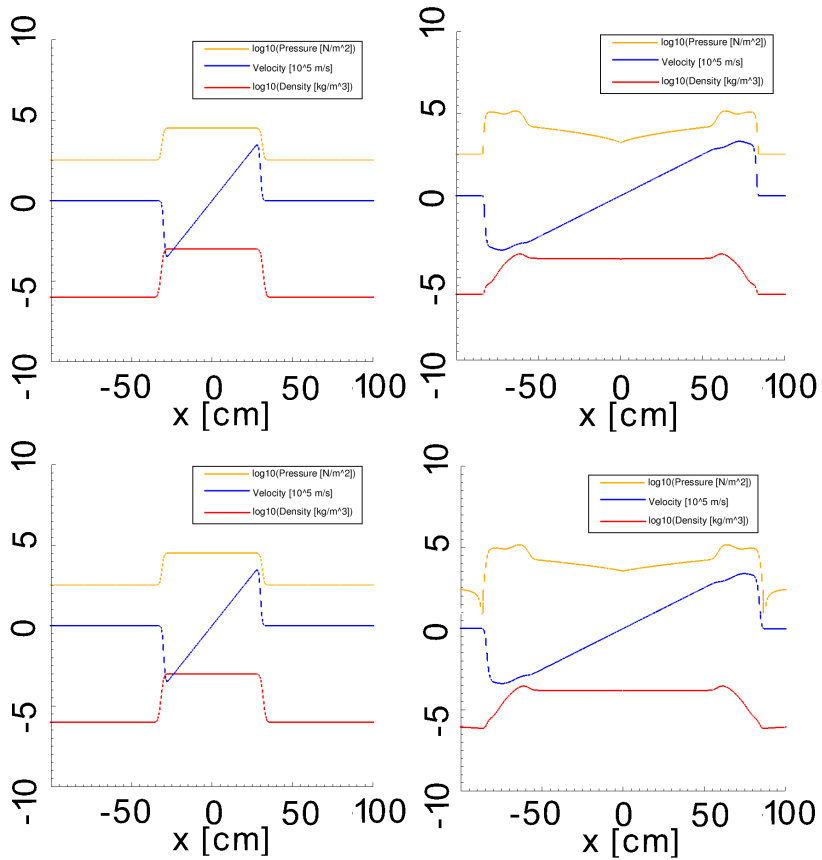


Figure 4.2.: Density, pressure and velocity along the x -axis for $t = 0 \mu\text{s}$ (left) and $t = 1.2 \mu\text{s}$ (right) for $B = 0.05$ T (top) and $B = 1$ T (bottom) (linear initialization)

A larger difference between the profiles in x and y directions is observed. The pressure shows the expected elongation along the direction of the magnetic field, whereas the velocity demonstrates a wider range along the y direction.

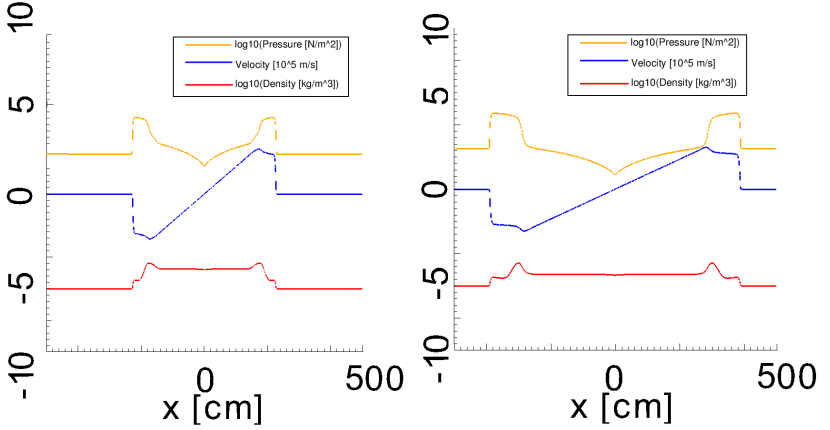


Figure 4.3.: Density, pressure and velocity along the x-axis for $t = 5 \mu\text{s}$ and $t = 10 \mu\text{s}$ for $B = 0.05 \text{ T}$ (linear initialization)

The profiles of thermodynamic properties along the y axis can be found in Fig. 4.5.

The expansion of the plasma along the y-axis shows no abrupt drop in velocity as opposed to the x-axis profile. An almost linear drop in velocity is observed which then stops at the edge of the transported fluid and is reduced to zero. Qualitatively, this transport perpendicularly to the magnetic field can be explained by the propagation of a fast magnetosonic wave as was mentioned in section 2.1.2. On the other hand, the propagation along the x direction is coupled with the presence of an Alfvén and a sound wave (Fig. 2.4), whose interaction leads to the observed undershooting in pressure.

The comparison of the two initialization procedures showed that they both exhibit numerical problems, however the linear initialization was preferred for the next simulations since it allowed a longer simulation time and represents a physically more realistic setup.

4. Results

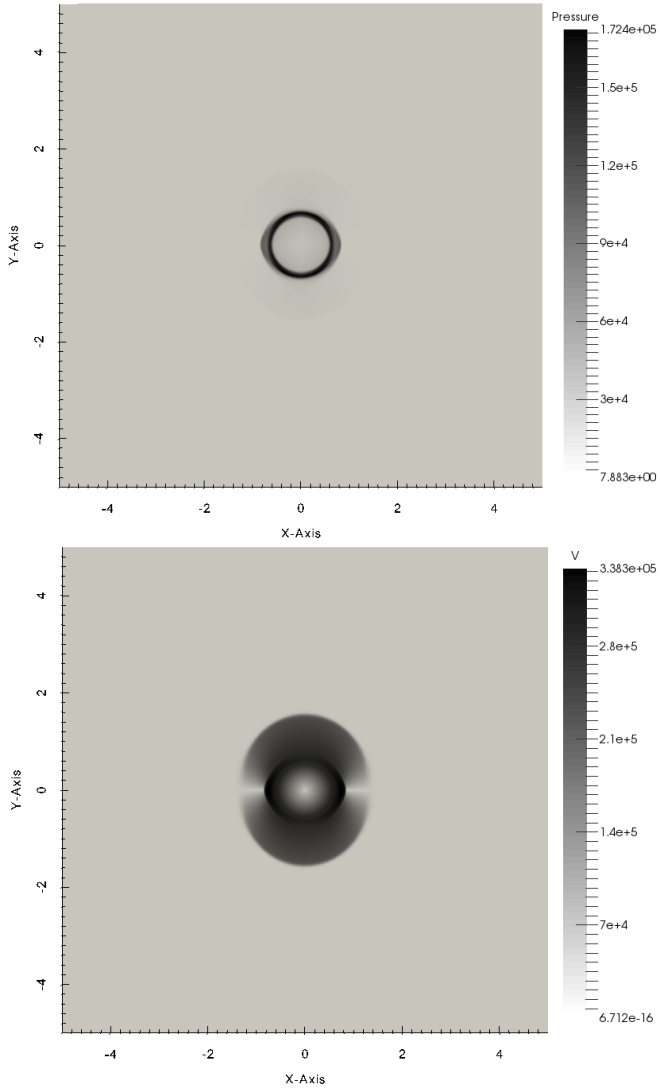


Figure 4.4.: Pressure and velocity distribution for $t = 1.2 \mu\text{s}$ and $B = 1 \text{ T}$ (linear initialization)

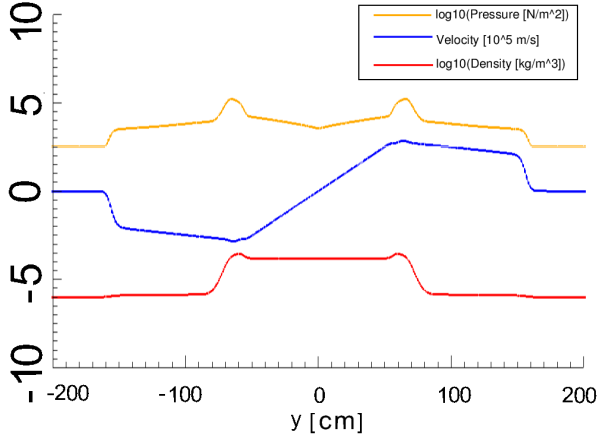


Figure 4.5.: Density, pressure and velocity along y -axis for $t = 1.2 \mu\text{s}$ and $B = 1 \text{ T}$ (linear initialization)

4.1.2. Modification of outer pressure

To reduce the source of the numerical undershooting in pressure without compromising the physical validity of the problem modeling, the outer pressure was modified. This served a double purpose: First, a higher outer pressure allows for larger undershoots. Secondly, the smaller pressure discontinuity reduces the gradient of the normal shock and also the interaction of the sound and Alfvén waves.

With the new value $p_{in}/p_{out} = 10$, the profiles in Fig. 4.6 were obtained. The negative pressure at the plasma edge was avoided and the smallest pressure value was shifted to the center of the domain. This configuration was adopted for the next simulations. Table 4.1 summarizes the properties used in this simulation.

4. Results

Table 4.1.: Initial Conditions for the linear profile domain initialization

Variable	Inside	Outside
Density	$\rho = 10^{-3} \text{ kg/m}^3$	$\rho = 10^{-6} \text{ kg/m}^3$
Pressure	$p = 3.25 \cdot 10^4 \text{ N/m}^2$	$p = 3.25 \cdot 10^3 \text{ N/m}^2$
Velocity	$v(r) = 3.433 \cdot 10^5 \text{ m/s} \cdot \frac{r}{0.3\text{m}}$	$v = 0 \text{ m/s}$
Magnetic field	$B = 1 \text{ T}$	$B = 1 \text{ T}$

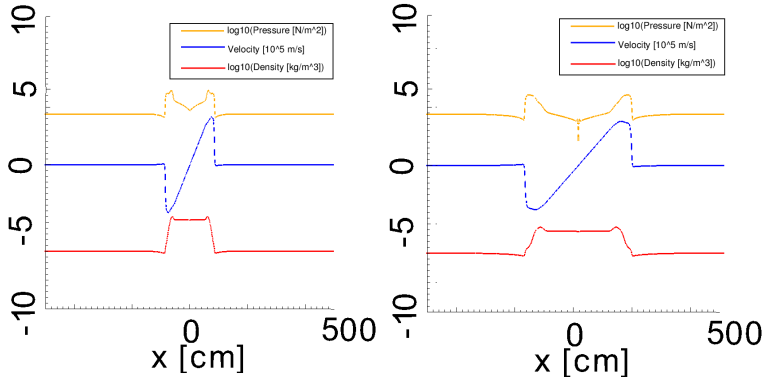


Figure 4.6.: Density, pressure and velocity along x-axis for $t = 1.2 \mu\text{s}$ and $t = 3.6 \mu\text{s}$ for $B = 1 \text{ T}$ (linear initialization for $p_{in}/p_{out} = 10$)

4.1.3. Presence of MHD waves

In order to evaluate the results with an external magnetic field, it is important to keep in mind the presence of the different waves in the MHD description of the problem. In section 2.1.2 the dependency of the wave phase velocities was shown as a function of the angle between the wave vector and the external magnetic field vector. In the case simulated in this section, the thermodynamic properties of the fluid outside of the energetic region lead to the characteristic velocities shown in Table 4.2 according to Eq. 2.18, Eq. 2.23 and Eq. 2.27. With this result, a dispersion curve similar to Fig. 2.4 was constructed and it

is shown in Fig. 4.7.

Table 4.2.: Characteristic velocities

v_S	$7.360 \cdot 10^4$ m/s
v_A	$8.902 \cdot 10^5$ m/s
v_M	$8.951 \cdot 10^5$ m/s

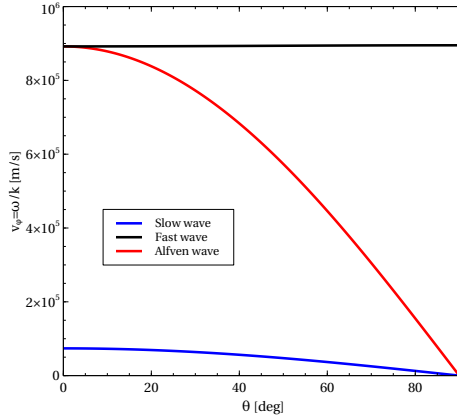


Figure 4.7.: Wave phase velocity as a function of the θ between wave vector and magnetic field

The magnitude of the speed of sound is small compared to the Alfvén speeds, as expected in vacuum. Moreover, it can be seen that the Alfvén and magnetosonic speeds exceed the fluid speed and hence a sub-Alfvénic flow is present. The maximal wave speed (v_M) was used in order to scale the dimensions of the computational domain. In order to avoid wave reflections at the edges of the domain, a radius bigger than 8.951 m is needed to ensure no reflection during the first 10 μ s of the simulation. For that reason a 20x20 domain was used in all calculations with magnetic field, as shown in Appendix C.

4.1.4. Effect of velocity

Due to the problems encountered when modeling the high external field with the presence of supersonic flows, the maximal speed was decreased to avoid shocks. Specifically, two cases with maximal speeds equal to $v_{max}/5$ and $v_{max}/10$ were examined, where v_{max} represents the nominal case presented previously. The profiles of the plasma properties along x and y directions for $t = 5 \mu s$ and $t = 10 \mu s$ are shown in Fig. 4.8, and Fig. 4.9.

The absence of the normal shock which was dominant in the results of section 4.1.1 can be observed. As expected, the case with higher velocity demonstrates a higher expansion as well, as the density plot shows. The plots along y direction prove however that the magnetosonic wave propagating through the medium is independent of the initial speed of the particles and is defined purely by the magnetic field vector and the density of the outer region. Comparing the wavefronts in Fig. 4.9, the wave propagation speed can be reconstructed and was found to coincide with the value in Table 4.2 within the measurement uncertainty limits.

Another important effect observed is the evolution of the velocity along the y direction. This velocity is perpendicular to the “frozen” external field lines and therefore increases their curvature and hence the magnetic tension. This restoring force acts as described in Fig. 2.2 and can exceed the inertia of the fluid, thereby changing its direction of motion. This effect is observed at $t = 10 \mu s$ (Fig. 4.9), where the components of y velocity seem to change sign. As expected, a lower speed results to a smaller inertia and that is the reason why the $v_{max}/10$ case shows an amplification of this phenomenon. A visual representation of the magnetic field lines curvature is given in Fig. 4.10.

The 2D contour plots for the density, pressure and velocity at $t = 10 \mu s$ for both velocity values is given in Fig. 4.11. In the velocity plot, it is evident that the wavefront of the fast wave is close to the edge of the domain. It is also seen that it has reached almost the same distance independently of the expansion direction, i.e. independently from the angle θ between the wave vector and the magnetic field lines. This coincides with the prediction shown in Fig. 4.7, where the speed of propagation of the fast wave was found to be almost equal for all angles, due to the relatively small speed of sound. The intensity of the

4.1. Constant magnetic field

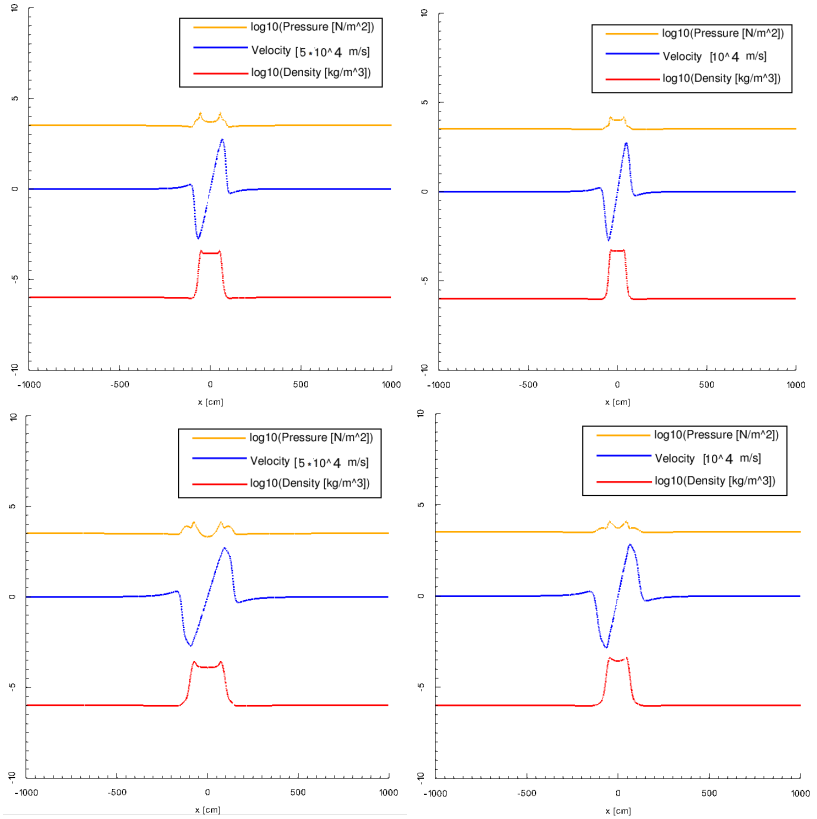


Figure 4.8.: Plots along x-axis for maximal speed $v_{max}/5$ (left) and $v_{max}/10$ (right) at $t = 5 \mu\text{s}$ (top) and $t = 10 \mu\text{s}$ (bottom) for $B = 1$ T (linear initialization)

wave (identified by the width in the contour plot) is not constant for all angles and has its maximum along the y direction (90 degrees), whereas it drops to zero along the x-axis ($\theta = 0$).

4. Results

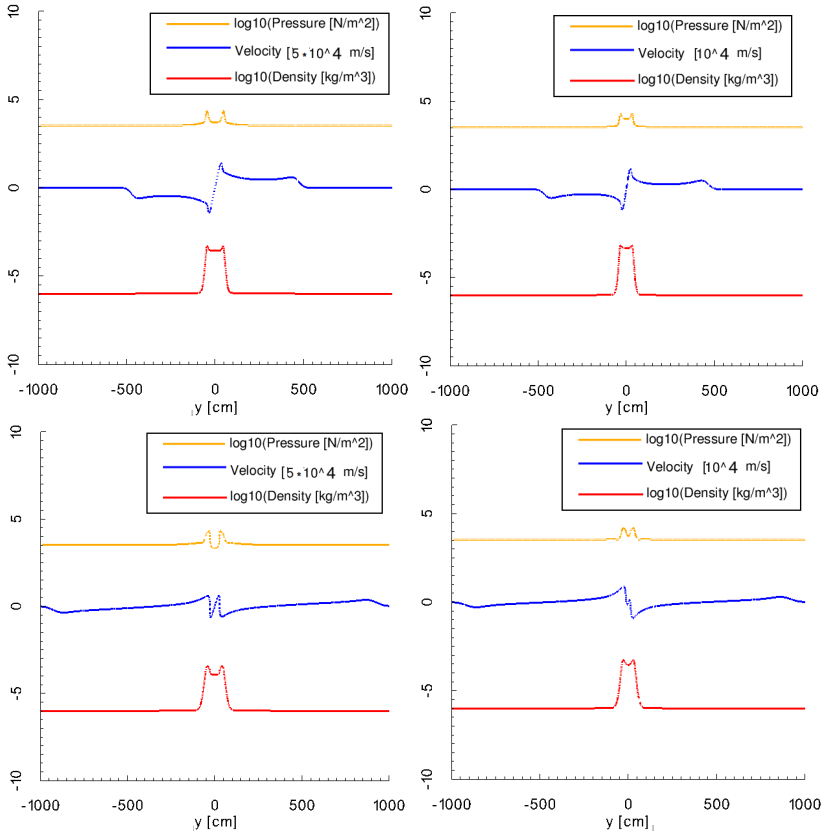


Figure 4.9.: Plots along y-axis for maximal speed $v_{max}/5$ (left) and $v_{max}/10$ (right) at $t = 5 \mu\text{s}$ (top) and $t = 10 \mu\text{s}$ (bottom) for $B = 1 \text{ T}$ (linear initialization)

4.1.5. Efficiency of nozzle

In order to achieve a quantification of the effect that the magnetic field has in the thrust performance, the efficiency of the configuration has to be obtained.

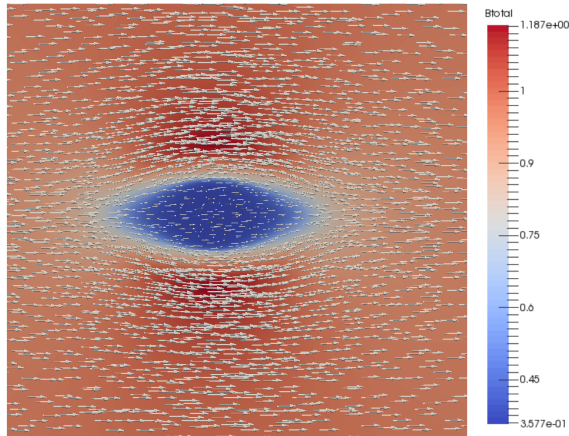


Figure 4.10.: Magnetic field vector plot for $v_{max}/5$ at $t = 7.5 \mu s$ and $B = 1 \text{ T}$ (Linear Initialization)

However, in the case of a uniform magnetic field, the net impulse in the x direction (the desired thrust direction) will remain equal to 0, due to the symmetry of the problem. For that reason, only the half xy plane was observed in order to come up with an equivalent efficiency. A net x-impulse is found by integrating the momentum over the half plane ($x > 0$) yielding an equivalent efficiency as in Appendix B.

The efficiency is plotted for an increasing magnetic field strength in Fig. 4.12. For small values of the field strength, a rapid increase in the efficiency was observed. However for higher values of B , the efficiency saturates towards the theoretical maximum of $\eta_{nozzle} = 1$. Moreover, it was validated that a smaller initial velocity resulted in a bigger efficiency. This effect comes from the smaller inertia of the fluid, which makes it easier to be redirected by the external field.

4. Results

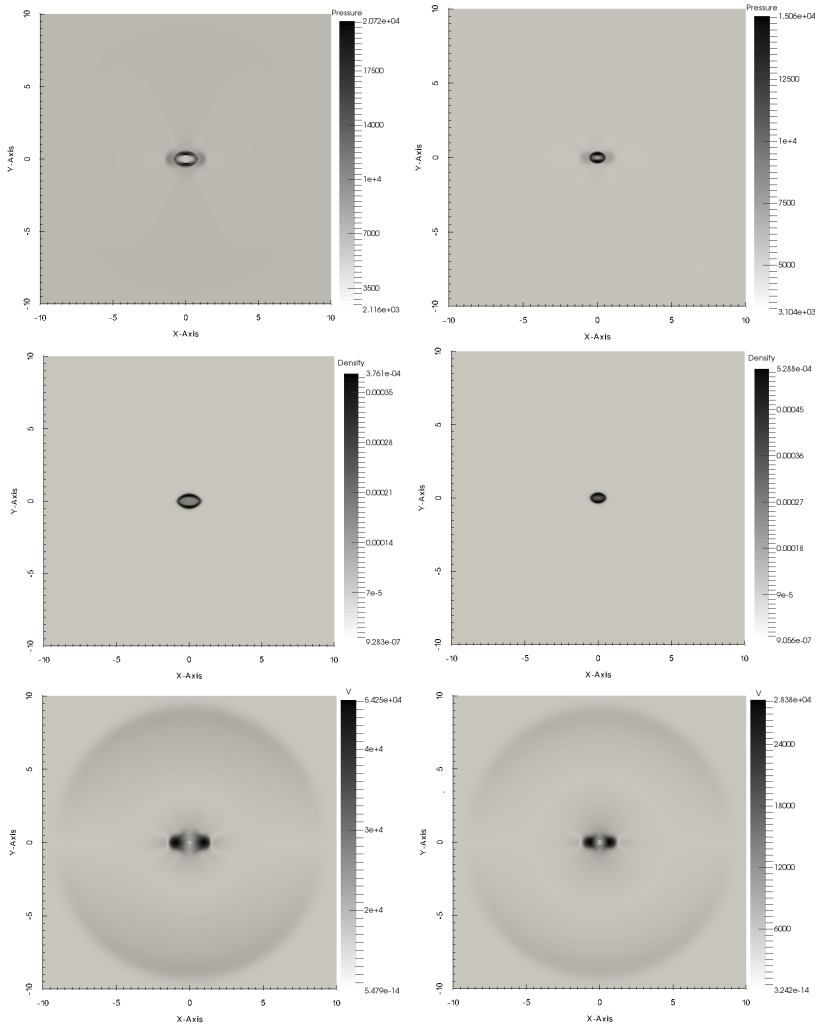
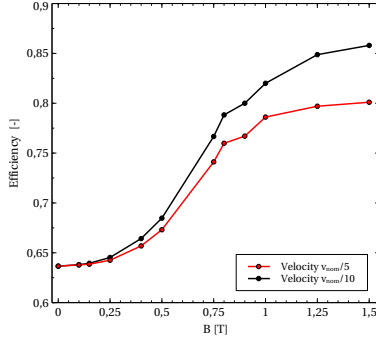


Figure 4.11.: Pressure, density and velocity distribution for $v_{max}/5$ and $v_{max}/10$ at $t = 10 \mu s$ and $B = 1 T$ (linear initialization)

Figure 4.12.: Efficiency over magnetic field strength at $t = 10 \mu\text{s}$

4.2. Coil magnetic field

In order to simulate the movement of the plasma in the presence of an electromagnetic coil, the magnetic field created by a single coil was computed using the Biot-Savart law [8]. The simulated configuration consists of a single circular coil with radius R_c , located at position $\mathbf{r}_0 = (x_0, y_0, z_0)^T$. The symmetry axis of the coil is parallel to the x-axis and a constant current with magnitude I is flowing through the superconducting coil. The magnetic field strength \mathbf{B} at the location $\mathbf{r} = (x, y, z)^T$ is given by

$$\mathbf{B}(\mathbf{r}) = \frac{\mu_0 I}{4\pi} \int_C \frac{d\mathbf{l} \times (\mathbf{r} - \mathbf{r}_c)}{|\mathbf{r} - \mathbf{r}_c|^3}, \quad (4.1)$$

where \mathbf{r}_c represents the location of a single point on the coil and $d\mathbf{l}$ an infinitesimal piece of the coil, directed along the current flow. For the first simulation, the values described in [27] were used in order to obtain an estimate of the entities' order of magnitude. This way the coil with $R_c = 1$ m was placed at $\mathbf{r}_0 = (-1, 0, 0)^T$ m and allowed a current $I = 3.56$ MA to pass through it. The magnetic field strength was calculated numerically and the resulting profile is shown in Fig. 4.13.

The calculation of $\mathbf{B}(\mathbf{r})$ was validated using the analytical solution obtained

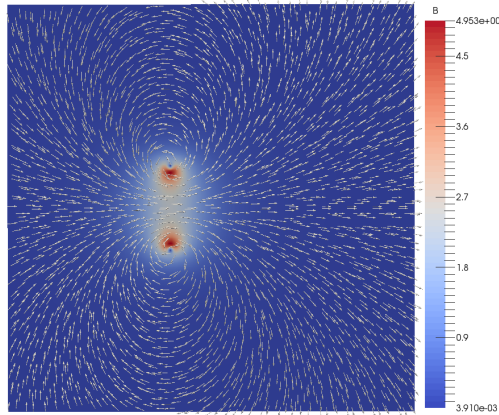


Figure 4.13.: Contour plot of magnetic field strength: Arrows represent the direction and the colormap the magnitude of the field strength

with the use of elliptical integrals [8]. The profile of the field’s magnitude along the symmetry axis of the coil is illustrated in Fig. 4.14. Along this axis, the maximal value is observed at the center point of the coil and it coincides with the expected analytical solution

$$|\mathbf{B}(-1, 0, 0)| = \frac{\mu_0 I}{2R} = 2.237 \text{ T} \quad (4.2)$$

Along the radial direction of the coil, the field strength density increases for distances closer to the conductor position. A plot of the profile of the field strength along the vertical position is given in Fig. 4.15. The theoretical value at the position of the coil approaches infinity but serves no physical purpose for the present simulation. Without any special treatment, the maximal field strength is limited due to the finite mesh of the domain and hence reaches values close to 5 T as shown in Fig. 4.15.

A summary of the initial conditions as resulted from the previous chapters can be seen in Table 4.3. It was evident from the first simulation, that the region

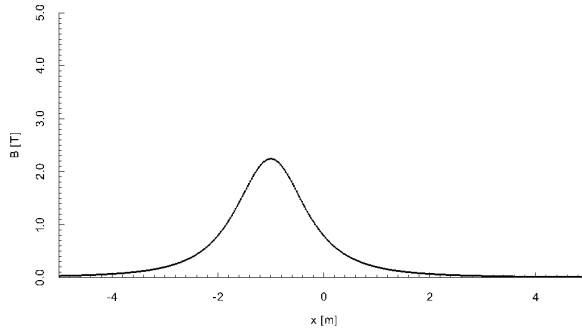


Figure 4.14.: Plot of the magnetic field strength along the symmetry axis of the coil

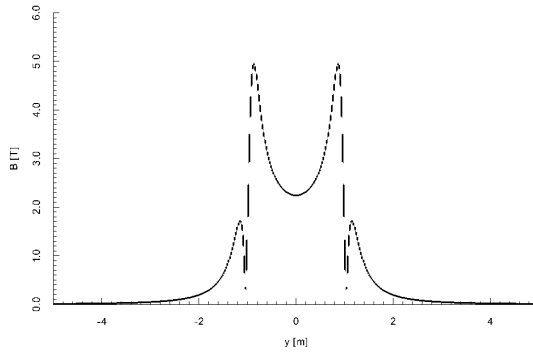


Figure 4.15.: Plot of the magnetic field strength along the radial axis of the coil

close to the coil would need special treatment. Specifically, the pressure near

4. Results

the two conductor positions exhibits again negative values. A contour plot of the pressure after 0.8 s is given in Fig. 4.16. The numerical undershooting in the pressure occurs when the fast wave arrives at the location of the coil and the transported pressure profile encounters the big field gradient.

Table 4.3.: Initial conditions for coil simulation

Variable	Inside	Outside
Density	10^{-3} kg/m^3	10^{-6} kg/m^3
Pressure	$3.25 \cdot 10^4 \text{ N/m}^2$	$3.25 \cdot 10^3 \text{ N/m}^2$
Velocity	$2.697 \cdot 10^4 \text{ m/s} \frac{r}{0.3 \text{ m}}$	0 m/s
Magnetic field	Coil field	Coil field

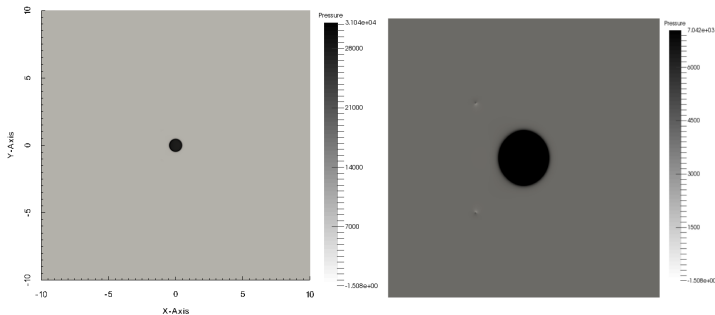


Figure 4.16.: Contour plot of pressure with zoom-in for $t = 0.8 \mu\text{s}$

4.2.1. Sponge layer

In order to induce a damping of the pressure oscillation, a sponge layer was implemented [2] which was placed at the location of the conductor. This method damps the conservative state to the background value, to exclude the coil from the solution. Different parameters were utilized in order to find the optimal

radius and dampening degree of the sponge layer. It was observed that longer simulation durations were allowed after this treatment, however the code was not prevented from crashing. Specifically, a drop in pressure and an extreme increase in velocity was observed at the edge of the sponge layer. A case where the radius of the sponge was set equal to 0.5 m is shown in Fig. 4.17, Fig. 4.18 and Fig. 4.19.

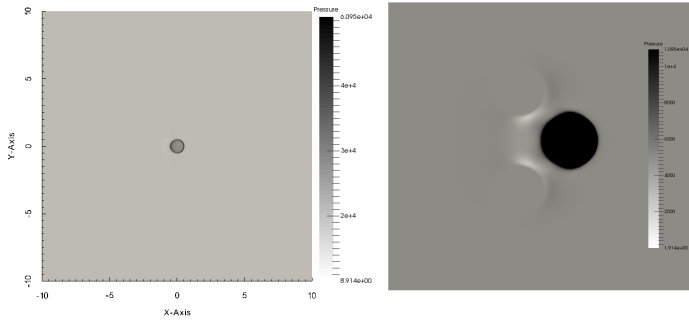


Figure 4.17.: Pressure distribution with zoom-in for $t = 2.6 \mu\text{s}$ (Sponge Layer)

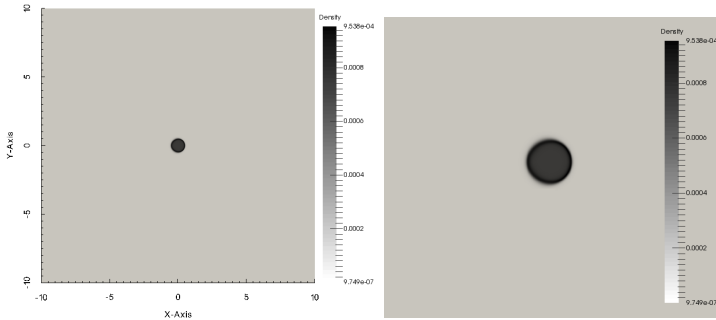


Figure 4.18.: Density distribution with zoom-in for $t = 2.6 \mu\text{s}$ (Sponge Layer)

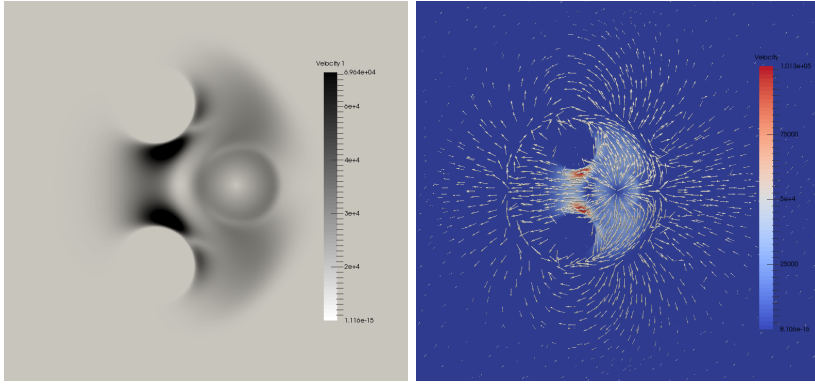


Figure 4.19.: Velocity distribution and vector plot with zoom-in for $t = 2.6 \mu\text{s}$ (Sponge Layer)

One can observe that the plasma still possesses a small expansion dimension due to the small timescale and hence no physical collision between the energetic plasma particles and the coil/sponge is taking place. The disturbance is triggered by the propagation of the MHD waves, which could not be resolved by the sponge. The vector plot in Fig. 4.19 shows that outside of the critical region the flow is as expected, with ions following the magnetic field lines and being compressed at the locations of maximal field strength (symmetry point of the coil).

4.2.2. Geometry modification

The observed issues with the pressure and the velocity are mainly triggered due to the interaction between the MHD waves and the high magnetic field gradients close to the coil. In order to suppress this phenomenon (since it provides no physical information for the simulated system), the coil was placed further away from the origin of the explosion.

The distance of the coil symmetry point from the origin was increased by a factor of 4 and so did the radius R_c . In order to preserve the field strength of the configuration, the current through the coil had to be increased by the same

factor, leading to $I = 14.24$ MA.

With these properties a bigger time evolution of the system was allowed, reaching a physical time equal to $t = 7.42 \mu\text{s}$. Fig. 4.21 illustrates that the minimal pressure occurs at the plasma edge and not at the location of the conductor. Although a slight pressure decrease is observed at the sponge layer, the drop at the plasma edge is more dominant. This undershooting takes place at the location of the plasma which is the closest to the coil, since the field strength has a bigger value and leads to a higher fast wave speed and to an increased pressure wave amplitude. The decreased pressure leads to an increase in velocity as seen in Fig. 4.20. The density in Fig. 4.21 demonstrates a small elongation along the x direction, proving that a net thrust is starting to build up.

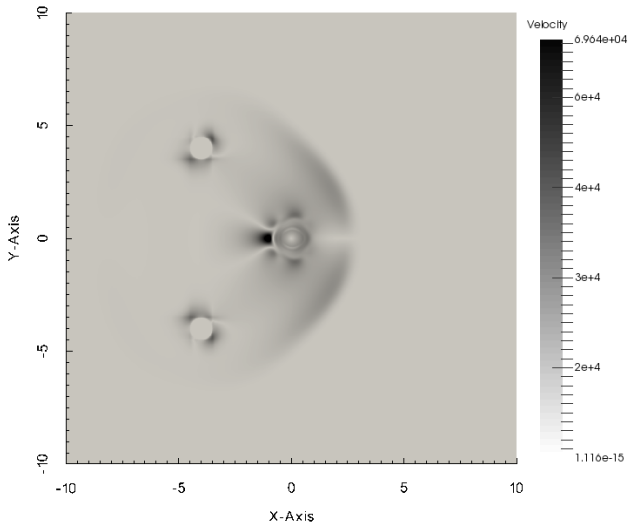


Figure 4.20.: Velocity distribution for $t = 7.42 \mu\text{s}$ (Sponge Layer with bigger coil dimension)

4. Results

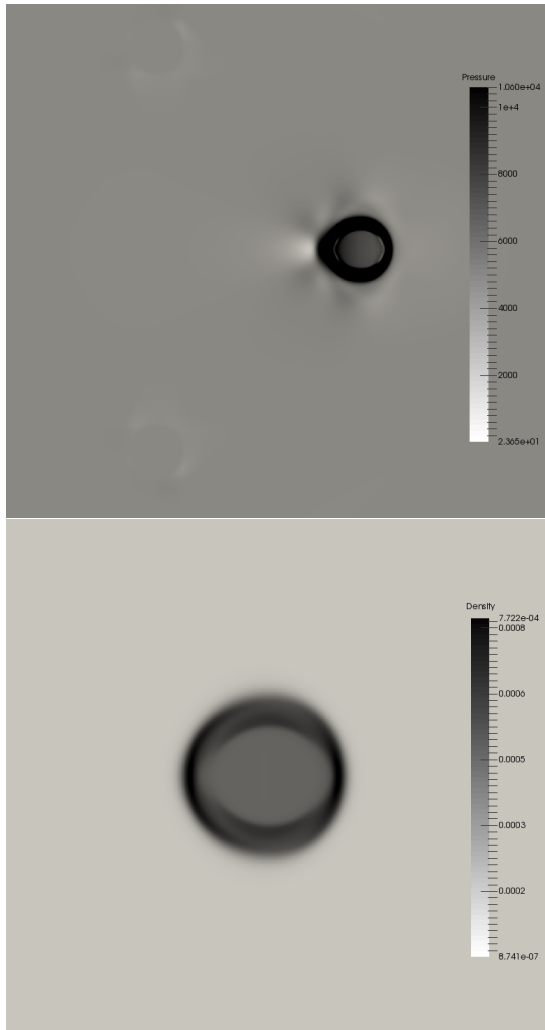


Figure 4.21.: Pressure (top) and density (bottom) distribution (zoom-in) for $t = 7.42 \mu\text{s}$ (Sponge Layer with bigger coil dimension)

Higher pressure

Finally, an effort was made to suppress the negative pressure in the fluid by equalizing the initial pressure all over the domain, while preserving the modified geometry. According to this assumption, the relationship $p_{out} = p_{in} = 3.25 \cdot 10^4 \text{ N/m}^2$ holds. Although this condition does not represent the physical case realistically for reasons explained in Section 3.3, it was implemented for the purpose of reducing the numerical issues.

The results at $t = 11 \mu\text{s}$ are shown in Fig. 4.22 and Fig. 4.23 and demonstrate complicated shock and wave interactions leading again to a negative pressure.

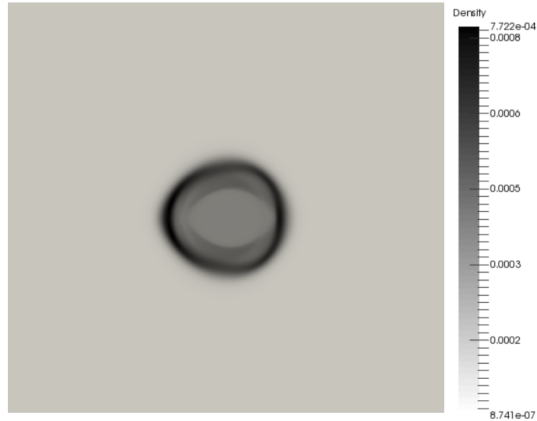


Figure 4.22.: Density distribution (zoom-in) for $t = 11 \mu\text{s}$ (Sponge Layer with bigger coil dimension and higher pressure)

Although the resolution of the steep gradients and pressure decrease was not successful for an examination of the efficiency for bigger time scales, the small simulation time period was examined with respect to the engine performance. Fig. 4.24 shows the time dependency of the efficiency for the coil geometry with increased dimensions.

4. Results

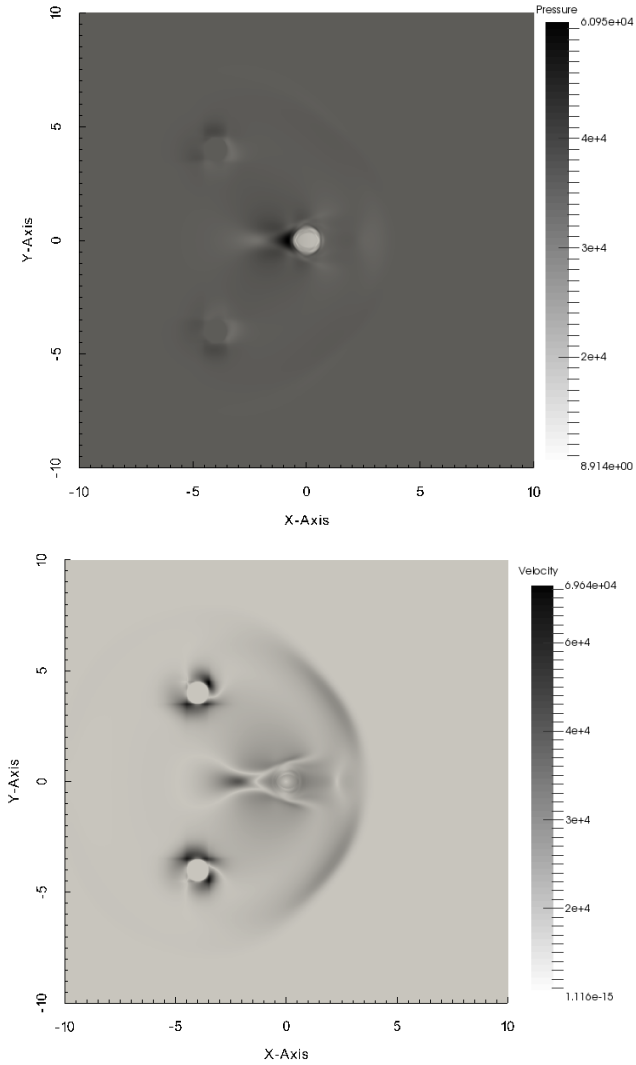


Figure 4.23.: Pressure (top) and velocity (bottom) distribution for $t = 11 \mu\text{s}$ (Sponge Layer with bigger coil dimension and higher pressure)

The difference between the two different pressure cases is minimal but as expected, the higher pressure demonstrates a slightly better performance. This is caused by the fact that the increased thermodynamic energy of the vacuum favours interactions with the energetic particles, thereby reducing their speed and allowing the magnetic field to redirect them more effectively due to the smaller inertia. The values are small in magnitude (maximal 1 % after 11 μs), demonstrate however a big time gradient thereby suggesting that they are far from their saturation region.

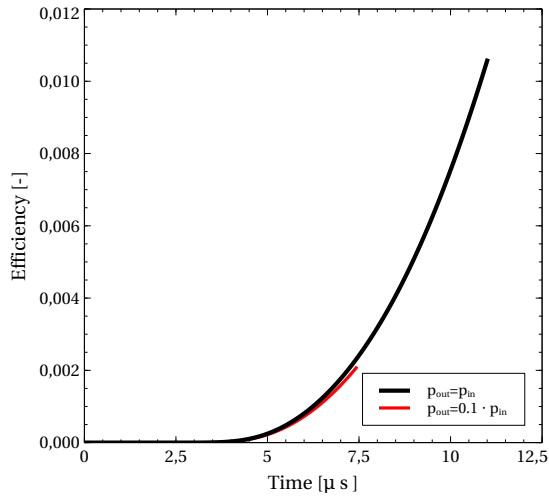


Figure 4.24.: Efficiency of the engine for single coil

5. Conclusion

The purpose of this work was to simulate a fusion plasma thruster and to investigate the modeling of the physical effects when using the ideal MHD equations. Fusion thrusters make use of the kinetic energy released during fusion processes by redirecting the ion products for the generation of thrust. The potential use of fusion thrusters in future interstellar missions calls for the presence of different techniques which can be used for their simulation.

Based on existing works which utilized different physical and numerical models (PIC, hybrid, SPH), typical initialization parameters of the plasma properties can be derived. Since the processes of ignition and hydrodynamic expansion after the fusion reaction do not belong to the topic of this work, conditions with macroscopic plasma expansion are chosen as initial conditions for the simulation. For the applications considered, the plasma properties are characterized by very high speeds resulting from the fusion process.

In order to compare the simulations with literature, the plasma properties have to be modified to suit the ideal MHD model without compromising the physical integrity of the problem. However it is found that certain parameters like the charge of the ions lack sufficient modeling in the ideal MHD case and hence could alter the underlying physical principles. On the other hand, thermodynamic properties which do not require modeling in particle methods, need special treatment in the case of ideal MHD. A disadvantage of the chosen model lies in the representation of the vacuum conditions in a way that does not induce numerical instabilities but still does not affect the integral quantities.

With the modified initial conditions, results for the expansion of the plasma in the present of a constant magnetic field can be obtained. The influence of the magnetic field strength on the efficiency of the nozzle is examined and shows that an increased field strength also improves the thrust performance. Similar results yield from the examination of a coil magnetic field, where a time dependent increase in the efficiency is observed and quantified. The model of MHD also captures the movement of plasmas for a wider range of velocities

5. Conclusion

and demonstrates better results in the case of lower speeds.

Due to the fact that the plasma is modeled as a fluid, the presence of waves is unavoidable when examining solutions with a strong external magnetic field. Although these waves represent physical phenomena which are existent in plasmas satisfying the MHD assumptions, their resolution triggers numerical instabilities. Moreover, the 1st order FVM which was implemented for the calculations is the one with the highest stability due to its dissipative nature but still cannot avoid all numerical problems. It is expected that higher order schemes would lead to even higher instabilities.

It is also evident, that physical structures and regions with high magnetic field gradients like the conductor coils used in magnetic nozzles, require special treatment to moderate the solution in their vicinity. Although efforts were made to diminish these unwanted effects, no results could be obtained for the thrust performance for larger time scales.

Ideal MHD is an attractive modeling tool for plasma applications due to its relatively simple formulation. It is shown to provide qualitatively correct solutions in the case of fusion thruster modeling as far as redirecting the plasma in the magnetic nozzle is concerned. However, due to the induced complexity resulting from the wave propagation and extreme pressure rarefactions in the presence of high speeds and magnetic field strengths, its effectiveness is considered to be less than in the case of particle-based and hybrid methods.

Since most presented disadvantages are connected to numerical issues, special treatments of the strong gradients could pose a suitable solution without the need of changing the underlying physics. Another possible suggestion would be to extend the model to include viscous effects (resistive MHD) and to examine which effects can be subsided with this formulation. In general, the physical description of the problem is sufficient in the case of MHD and is able to provide results for smaller speeds and time scales, which implies that with proper treatment of the numerical issues, a complete description of variable plasma thruster configurations could be achieved.

A. 1D Simulation of velocity discontinuity

In Section 3.2, the effect of a uniform disc initialization was examined. It was mentioned that according to Toro [36], a numerical vacuum condition is obtained at the origin of the velocity discontinuity. Specifically, Toro performs a shock tube simulation with different gas dynamic conditions for the fluid at right and left parts of the domain as described in Table A.1.

Table A.1.: Initial Conditions defined in [36]

Property	Left	Right
Velocity	-0.2	0.2
Pressure	0.4	0.4
Density	1.0	1.0

The results of the simulation after 0.15 time units are shown in Fig. A.1.

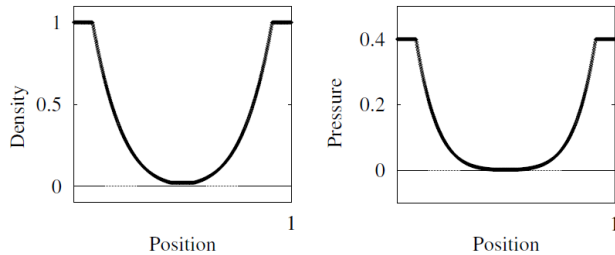


Figure A.1.: Density and pressure plots for 1-D gas dynamic shock tube simulation [36]

In order to verify the process for the values used in Section 3.2, a 1D simulation

A. 1D Simulation of velocity discontinuity

was set up with the initialization shown in Fig. A.2

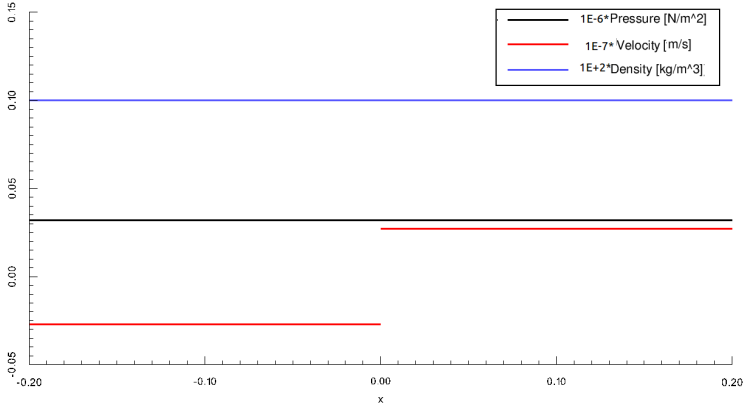


Figure A.2.: Initial conditions of the 1-D Simulation

The solution of the 1D shock tube expansion problem lead to a sharp decrease in the pressure and density as illustrated in Fig. A.3. The values of the thermodynamic properties close to the origin are close to zero and therefore the numerical issues triggered by this type of initialization are clearly demonstrated.

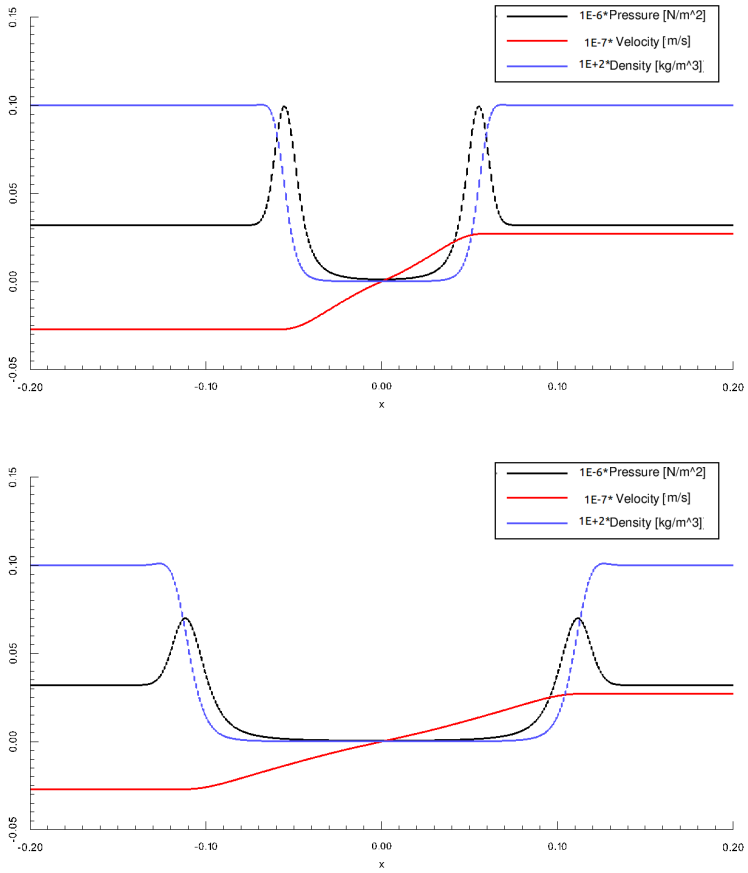


Figure A.3.: Density, pressure and velocity plots for 1D gas dynamic shock tube simulation after 2 μs and 4 μs

B. Calculation of efficiency for constant field

In Section 4.1, the efficiency of the nozzle was examined in the case of a constant magnetic field. In the case of an isotropic expansion and a uniform magnetic field, the net impulse in the x direction (the desired thrust direction) becomes zero. For that reason, only half of the domain was examined in order to quantify the compression that the magnetic field causes.

The net impulse in the x direction is hence positive even in the case of a uniform expansion in the absence of an external field. The value of this equivalent efficiency for the isotropic case is easily obtained by taking into account the sketch in Fig. B.1.

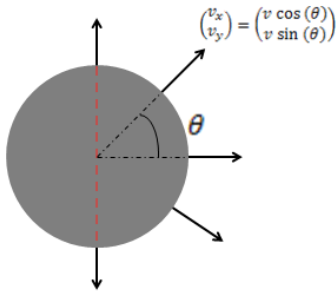


Figure B.1.: Isotropic expansion and velocity vectors

The velocity of each element can be described by the vector $(v_x, v_y)^T = (v \cdot \cos(\theta), v \cdot \sin(\theta))^T$. The magnitude of the velocity is $v = \sqrt{v_x^2 + v_y^2}$. Since only the region for $x > 0$ is of concern, θ takes values between $-\pi/2$ and $\pi/2$. The efficiency according to Eq. 1.12 becomes

B. Calculation of efficiency for constant field

$$\eta_{nozzle} = \frac{\int \rho v_x dV}{\int \rho v dV} = \frac{r^2/2 \int_{-\pi/2}^{\pi/2} \rho v \cos(\theta) d\theta}{r^2/2 \int_{-\pi/2}^{\pi/2} \rho v d\theta} = \frac{2}{\pi} \approx 0.63662 \quad (\text{B.1})$$

It is therefore expected that a magnetic field along the positive x direction will always provide values for this equivalent efficiency higher than 0.63662.

C. Meshes

The domain used in the simulations consisted of a stretched mesh as shown in Fig. C.1 and Fig. C.2. The depicted mesh consists of 100 nodes in each direction whereas the mesh used throughout the simulations was made up of 800 nodes in each direction. The dimensions of the mesh were chosen to be 10x10 meters in the cases without external field. For the simulations with external magnetic field, the dimensions of the mesh were changed to 20x20 meters as explained in Section 4.2 and the number of elements along each direction was also doubled leading to 1600x1600, whereas the stretch parameters were kept equal.

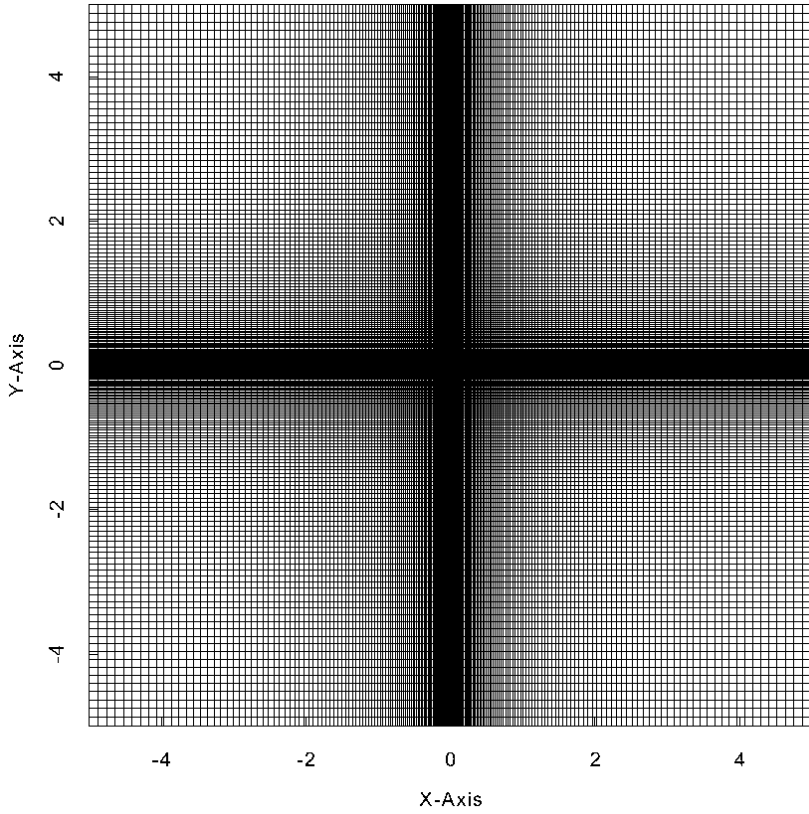


Figure C.1.: Stretched mesh with 100x100 elements

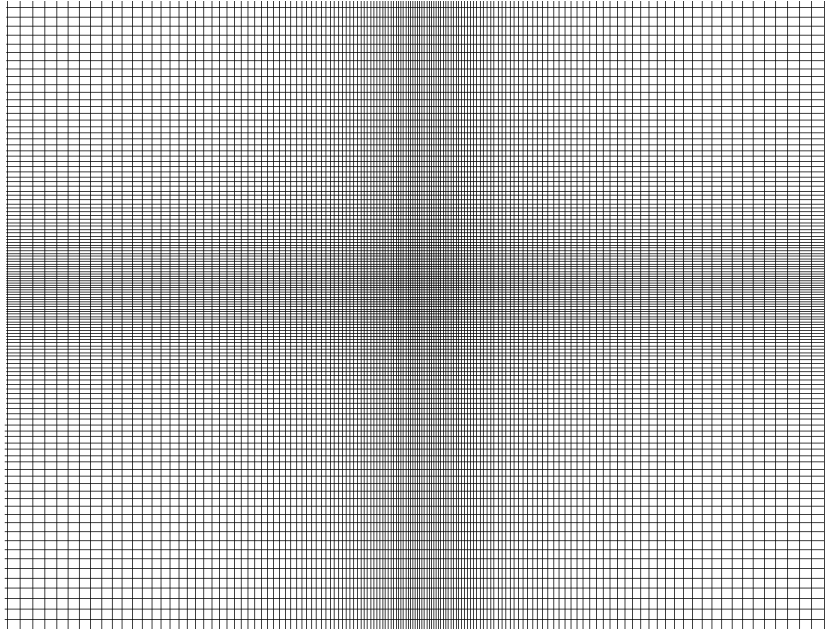


Figure C.2.: Zoom of the stretched mesh with 100x100 elements

Bibliography

- [1] The Daedalus Project. *Acta Astronautica*, 49(3–10):555 – 556, 2001.
- [2] M. K. A. Babucke, J. Linn and U. Rist. Direct numerical simulation of shear phenomena on parallel vector computers. *High Performance Computing on Vector Systems*, 2006.
- [3] E. Ahedo and M. Merino. On plasma detachment in propulsive magnetic nozzles. *Physics of Plasmas*, 18(5), 2011.
- [4] S. Andersen, V. Jensen, P. Nielsen, and N. D’Angelo. Continuous supersonic plasma wind tunnel. *Physics of Fluids*, 12(3):557–560, 1969.
- [5] S. Atzeni and J. M. ter Vehn. *The Physics of Inertial Fusion*. 1st edition, 2009.
- [6] P. A. Davidson. *An Introduction to Magnetohydrodynamics*. Cambridge University Press, 1st edition, 2001.
- [7] G. A. S. B. D. G. Gaidos, R. A. Lewis and S. Chakrabarti. Antiproton-catalyzed microfission/fusion propulsion systems for exploration of the outer solar system.
- [8] D. J. Griffiths. *Introduction to Electrodynamics (3rd Edition)*. Benjamin Cummings, 1998.
- [9] X. Guo. An extended hllc riemann solver for the magneto-hydrodynamics including strong internal magnetic field. *Journal of Computational Physics*, 290(0):352 – 363, 2015.
- [10] O. A. H. H. S. Park and J. D. Salmonson. High-adiabat high-foot inertial confinement fusion implosion experiments on the national ignition facility. *Physical Review Letters*, 112:52–57, 2014.
- [11] A. Hansson. Project Orion: The Atomic Spaceship 1957–1965. *Space Policy*, 19(2):149 – 150, 2003.

- [12] F. Hindenlang, G. Gassner, C. Altmann, A. Beck, M. Staudenmaier, and C.-D. Munz. Explicit discontinuous galerkin methods for unsteady problems. *Computers & Fluids*, 61:86–93, 2012.
- [13] J. D. Huba. *NRL Plasma Formulary*. Office of Naval Research, 2006.
- [14] A. E. Hubbard. Advances in burning plasma-related physics and technology in magnetic fusion. Presentation at the Fusion Energy Symposium 2013.
- [15] R. A. Hyde. A laser-fusion rocket for interstellar propulsion. *International Astronautical Federation*, 1983.
- [16] K. Ikeda. ITER on the road to fusion energy. *Nucl. Fusion*, 50, 2010.
- [17] S. Jardin. *Computational Methods in Plasma Physics*. CRC Press, 2010.
- [18] P. K. Kaw and I. Bandyopadhyay. *Fusion Physics, IAEA 2012*, chapter 1, pages 1–51.
- [19] M. Keilhacker and the ASDEX TEAM. The ASDEX divertor tokamak. In *Proceedings of 8th International Conference on Plasma Physics and Controlled Nuclear Fusion Research*, 1980.
- [20] R. Kodama. Nuclear fusion: Fast heating scalable to laser fusion ignition. *Nature*, 418:933–934, 2002.
- [21] J. D. Lawson. Some criteria for a power producing thermonuclear reactor. *Proc. Phys. Soc. B*, 70, 1957.
- [22] R. J. LeVeque. *Finite Volume Methods for Hyperbolic Problems*. Cambridge University Press, 2002.
- [23] K. Long, R. Obousy, and A. Hein. Project Icarus: Optimisation of nuclear fusion propulsion for interstellar missions. *Acta Astronautica*, 68(11–12):1820 – 1829, 2011.
- [24] C. A. R. M. D. Rayman, T. C. Fraschetti and C. T. Russel. Dawn: A mission in development for exploration of main belt asteroids Vesta and Ceres. *Acta Astronautica*, 58:605–616, 2006.

- [25] Y. K. N. Matsuda, A. Maeno and H. Nakashima. A magnetic thrust chamber design for a laser fusion rocket based on impact fast ignition scheme. *Plasma Fusion Res. Series*, 8, 2009.
- [26] Y. K. N. Sakaguchi and H. Nakashima. Thrust efficiency calculation for magnetic nozzle in laser fusion rocket. *Trans. Japan Soc. Aero. Space Sci.*, 48(161):180–182, 2005.
- [27] Y. Nagamine and H. Nakashima. Analysis of plasma behaviour in a magnetic thrust chamber of a laser fusion rocket. *Fusion Technology*, 35, 1999.
- [28] S. Pflanzner. *An introduction to Inertial Confinement Fusion*. Tylor and Francis, 1st edition.
- [29] O. Puyoo and L. B. Jaffel. The intrinsic properties of the local interstellar medium. *Lect. Notes Phys.*, 29, 1998.
- [30] Y. K. H. N. R. Kawabuchi, N. Matsuda and Y. P. Zakharov. Numerical simulation of plasma detachment from a magnetic nozzle by using fully particle-in-cell code. *Journal of Physics: Conference Series*, 112(4):042082, 2008.
- [31] V. Smirnov. Tokamak foundation in ussr/russia 1950-1990. *Nucl. Fusion*, 50, 2010.
- [32] G. P. Sutton and O. Biblarz. *Rocket Propulsion Elements*. John Wiley and Sons, Inc., 7th edition.
- [33] D. Swanson. Chapter 3 - Waves in fluid plasmas. In D. Swanson, editor, *Plasma Waves*, pages 77 – 118. Academic Press, 1989.
- [34] S. K. T. Harada and Y. Kawaguchi. Smoothed Particle Hydrodynamics on GPUs. *The Visual Computer*.
- [35] T. M. T. Kawasaki and H. Nakashima. Development of a MHD code using CIP method and its application to a laser fusion rocket. In *26th International Electric Propulsion Conference*, 1999.
- [36] E. Toro. *Riemann Solvers and Numerical Methods for Fluid Dynamics*. Springer, June 1999.

- [37] K. V. Vchivkov, H. Nakashima, F. Ichikawa, and Y. P. Zakharov. Optimization of thrust efficiency in laser fusion rocket by using three-dimensional hybrid particle-in-cell code. *Vacuum*, 73(3–4):427 – 432, 2004. The 4th International Symposium on Applied Plasma Science.
- [38] J. L. T. W. C. Elmore and K. M. Watson. On the Inertial-Electrostatic Confinement of a plasma. *The Physics of Fluids*, 2, 1959.
- [39] J. Wesson. *Tokamaks*. Clarendon Press, Oxford, 3rd edition, 2004.
- [40] P. J. Wisoff, E. G. V. B. D. F. Bowers, M. W., and D. R. Jedlovec. Nif injection laser system. In *Optical Engineering at the Lawrence Livermore National Laboratory II: The National Ignition Facility*, volume 5341 of *Society of Photo-Optical Instrumentation Engineers (SPIE) Conference Series*, pages 146–155, 2004.
- [41] G. A. Wurden. FRX-L: A plasma injector for Magnetized Target Fusion. Physics Division Research Review at Air Force Research Laboratory.
- [42] R. K. Y. Kajimura and H. Nakashima. Control techniques of thrust vector for magnetic nozzle in laser fusion rocket. *Fusion Engineering and Design*, 81:2871–2875, 2006.
- [43] C. D. Zhou and R. Betti. Hydrodynamic relations for direct-drive fast-ignition and conventional inertial confinement fusion implosions. *Physics of Plasmas*, 14(7), 2007.

List of Tables

2.1. MHD waves	19
3.1. Initial Conditions defined in [27]	28
3.2. Initial conditions for the parametric study of outside density influence	31
3.3. Initial Conditions for the parametric study of outside pressure influence	34
3.4. Initial Conditions for the uniform disc domain	37
3.5. Initial Conditions for the linear profile domain initialization . .	41
4.1. Initial Conditions for the linear profile domain initialization . .	52
4.2. Characteristic velocities	53
4.3. Initial conditions for coil simulation	62
A.1. Initial Conditions defined in [36]	73

List of Figures

1.1.	Lift-off of Ariane 5 rocket (Image from: www.esa.int)	2
1.2.	Dawn spacecraft's NSTAR electrostatic ion thruster (Image from: www.jpl.nasa.gov/)	3
1.3.	Overview of conventional space propulsion systems [32]	3
1.4.	Cross section of fusion reactions over ion temperature [13]	5
1.5.	Triple product as a function of temperature for the D-T, D-D , D-He3 reactions [13]	6
1.6.	Triple product as a function of time in comparison to Moore's law [14]	8
1.7.	Inside view of the ASDEX Upgrade Tokamak at the Max Planck Institute of Plasma Physics in Garching (Image from www.ipp.mpg.de)	9
1.8.	Mechanism of Inertial Confinement Fusion	9
1.9.	The inside of the ignition chamber at the National Ignition Facility (Image from www.extremetech.com)	10
1.10.	Animation of the indirect ICF method using a Hohlraum (Image from www.llnl.gov)	10
1.11.	Operating principle of magnetic nozzle [30]	11
2.1.	Magnetic tension forces along a field line [6]	18
2.2.	Perturbation of magnetic field line and restoring force [6]	19
2.3.	(Image from www.theory.physics.helsinki.fi) Magnetosonic wave compressing and releasing the lines of force and the conducting fluid perpendicularly to \mathbf{B}	20
2.4.	Phase velocity as a function of the angle between wave vector and magnetic field vector (Image from www.theory.physics.helsinki.fi)	20
2.5.	Finite Volume Method (Image from www.scielo.br)	22
2.6.	Finite Volumes Method time scheme	22
3.1.	Fusion Target and power profile for fast ignition ICF [43]	26
3.2.	Density and temperature profile along radius of pellet for fast ignition ICF [43]	27

3.3. Gas dynamic expansion at $t=10 \mu\text{s}$ for different density ratios ρ_{in}/ρ_{out}	32
3.4. Kinetic energy ratio (normalized to initial kinetic energy) along time for different density ratios ρ_{in}/ρ_{out}	33
3.5. Kinetic energy ratio (normalized to initial kinetic energy) along time for different pressure ratios p_{in}/p_{out}	35
3.6. Density contour plot during initialization [27]	36
3.7. Number density radial profile for $t = 1 \mu\text{s}$ [27]	36
3.8. Density, pressure and velocity profile for uniform disc initialization	37
3.9. Density, pressure and velocity distribution for the uniform disc initialization at $t = 0 \mu\text{s}$ (left) and $t = 10 \mu\text{s}$ (right)	39
3.10. Gas dynamic Mach number profile at $t = 10 \mu\text{s}$ for the uniform disc initialization	40
3.11. Density, pressure and velocity profile for linear initialization . .	42
3.12. Gas dynamic Mach number profile at $t = 10 \mu\text{s}$ (Linear Initialization)	43
3.13. Density, pressure and velocity distribution for the linear initialization at $t = 0 \mu\text{s}$ (left) and $t = 10 \mu\text{s}$ (right)	44
4.1. Density, pressure and velocity along the x-axis for $t = 0 \mu\text{s}$ (left) and at the final time step (right) for $B = 0.05 \text{ T}$ (top) and $B = 1 \text{ T}$ (bottom) (uniform disc initialization)	46
4.2. Density, pressure and velocity along the x-axis for $t = 0 \mu\text{s}$ (left) and $t = 1.2 \mu\text{s}$ (right) for $B = 0.05 \text{ T}$ (top) and $B = 1 \text{ T}$ (bottom) (linear initialization)	48
4.3. Density, pressure and velocity along the x-axis for $t = 5 \mu\text{s}$ and $t = 10 \mu\text{s}$ for $B = 0.05 \text{ T}$ (linear initialization)	49
4.4. Pressure and velocity distribution for $t = 1.2 \mu\text{s}$ and $B = 1 \text{ T}$ (linear initialization)	50
4.5. Density, pressure and velocity along y-axis for $t = 1.2 \mu\text{s}$ and $B = 1 \text{ T}$ (linear initialization)	51
4.6. Density, pressure and velocity along x-axis for $t = 1.2 \mu\text{s}$ and $t = 3.6 \mu\text{s}$ for $B = 1 \text{ T}$ (linear initialization for $p_{in}/p_{out} = 10$) . .	52
4.7. Wave phase velocity as a function of the θ between wave vector and magnetic field	53
4.8. Plots along x-axis for maximal speed $v_{max}/5$ (left) and $v_{max}/10$ (right) at $t = 5 \mu\text{s}$ (top) and $t = 10 \mu\text{s}$ (bottom) for $B = 1 \text{ T}$ (linear initialization)	55

4.9. Plots along y-axis for maximal speed $v_{max}/5$ (left) and $v_{max}/10$ (right) at $t = 5 \mu s$ (top) and $t = 10 \mu s$ (bottom) for $B = 1 T$ (linear initialization)	56
4.10. Magnetic field vector plot for $v_{max}/5$ at $t = 7.5 \mu s$ and $B = 1 T$ (Linear Initialization)	57
4.11. Pressure, density and velocity distribution for $v_{max}/5$ and $v_{max}/10$ at $t = 10 \mu s$ and $B = 1 T$ (linear initialization)	58
4.12. Efficiency over magnetic field strength at $t = 10 \mu s$	59
4.13. Contour plot of magnetic field strength: Arrows represent the direction and the colormap the magnitude of the field strength	60
4.14. Plot of the magnetic field strength along the symmetry axis of the coil	61
4.15. Plot of the magnetic field strength along the radial axis of the coil	61
4.16. Contour plot of pressure with zoom-in for $t = 0.8 \mu s$	62
4.17. Pressure distribution with zoom-in for $t = 2.6 \mu s$ (Sponge Layer)	63
4.18. Density distribution with zoom-in for $t = 2.6 \mu s$ (Sponge Layer)	63
4.19. Velocity distribution and vector plot with zoom-in for $t = 2.6 \mu s$ (Sponge Layer)	64
4.20. Velocity distribution for $t = 7.42 \mu s$ (Sponge Layer with bigger coil dimension)	65
4.21. Pressure (top) and density (bottom) distribution (zoom-in) for $t = 7.42 \mu s$ (Sponge Layer with bigger coil dimension)	66
4.22. Density distribution (zoom-in) for $t = 11 \mu s$ (Sponge Layer with bigger coil dimension and higher pressure)	67
4.23. Pressure (top) and velocity (bottom) distribution for $t = 11 \mu s$ (Sponge Layer with bigger coil dimension and higher pressure)	68
4.24. Efficiency of the engine for single coil	69
A.1. Density and pressure plots for 1-D gas dynamic shock tube simulation [36]	73
A.2. Initial conditions of the 1-D Simulation	74
A.3. Density, pressure and velocity plots for 1D gas dynamic shock tube simulation after $2 \mu s$ and $4 \mu s$	75
B.1. Isotropic expansion and velocity vectors	77
C.1. Stretched mesh with 100x100 elements	80
C.2. Zoom of the stretched mesh with 100x100 elements	81